MASTER IN ASTROPHYSICS AND SPACE SCIENCE

Erasmus Mundus Master
in Astrophysics and Space Science

Master Thesis

Pulsar timing around a supermassive black hole: Analytical calculations of propagation delay in Schwarzschild spacetime

Supervisors

PD Dr. Eva Hackmann
Centre of Applied Space Technology
and Microgravity,
University of Bremen.

Prof. Bojan Arbutina
Faculty of Mathematics,
University of Belgrade.

Author

Ifeoma Mavis Akpuogwu

February 2025

TOR VERGATA UNIVERSITÀ DEGLI STUDI DI ROMA
UNIVERSITY OF BELGRADE
University of Bremen
UNIVERSITÉ CÔTE D'AZUR
Funded by the European Union

This master thesis is submitted in partial fulfillment of the requirements for the degree **Master of Science** as part of multiple degrees awarded in the framework of the Erasmus Mundus Joint Master in Astrophysics and Space Science **MASS** jointly delivered by a Consortium of four Universities: Tor Vergata University of Rome, University of Belgrade, University of Bremen, and Université Cote d'Azur, regulated by the MASS Consortium Agreement and funded by the EU under the call ERASMUS-EDU-2021-PEX-EMJM-MOB.

Pulsar timing around a supermassive black hole: Analytical calculations of propagation delay in Schwarzschild spacetime

Abstract

The pulsar timing model, which compares the expected and actual arrival times of signals from a pulsar, would open the window for an accurate determination of black hole parameters and enable new tests of General Relativity (GR), especially in cases where a pulsar closely orbits the galactic center supermassive black hole, SgrA*. An important relativistic effect to consider in the timing model is the propagation delay in pulse arrival caused by the black hole's gravitational field. In this work, we derive an exact analytical formula for the propagation delay in a Schwarzschild spacetime, assuming the pulsar's mass is negligible compared to the supermassive black hole. Additionally, we obtain a solution for the angle of emission, φ. To evaluate the accuracy of existing models, we compare our result with three analytical approximations, particularly those proposed by Beloborodov, Poutanen and Beloborodov, and La Placa et al. While the first two approximations show deviations near superior conjunction, the third approximation is more reliable for edge-on orbits. We modify and assess the accuracy of the original k-values by fitting k_1, k_2, and k_3 for different radii and propose new values for the case we considered. Our findings indicate that for (nearly) edge-on orbits, the exact propagation delay formula should be used.

Keywords: Black holes – Light propagation – Pulsars – Pulsar timing

Contents

List of Figures

List of Tables

Chapter 1

Introduction

Supermassive black holes, like the one in our Milky Way galaxy are massive, highly dense objects located at the centers of most galaxies. Black holes with a mass of more than 10^5 solar masses ($M_\odot$) are classified as supermassive black holes; some black holes have masses as high as several billion $M_\odot$. Sagittarius A* (SgrA*) is the supermassive black hole hosted at the center of our galaxy with a mass of about 4×10^6 $M_\odot$[2, 3]. This supermassive black hole can be used to test for important features like the existence and shape of a black hole shadow[4, 5], the cosmic censorship conjecture[6], or the no-hair theorem[6–8]. The gravitational field of Sgr A* can be studied by observing the movement of nearby stars which would improve the accuracy of its mass estimate, its spin magnitude, and its corresponding orientation[6, 9]. An accurate determination of the black hole parameters, exploration of the gravitational field, and new tests of General Relativity (GR) would be possible by observing pulsars closely orbiting the supermassive black hole at the galactic center [10].

Pulsars are rapidly rotating neutron stars (NS) with stable rotation, giving radio emission, and about 10% with a companion[11]. These neutron stars are compact objects formed following the explosion of massive stars. Pulsars are classified into various types, including rotation-powered pulsars (RPP), magnetars, X-ray dim isolated neutron stars, accretion-powered neutron stars (such as X-ray bursters), and central compact objects[12, 13]. Pulsars can be isolated or in binary systems with white dwarfs, other neutron stars, etc[14]. Radio pulsars are neutron stars that emit beams of radio waves, observed as regular pulses corresponding to their rotation period. Their broadband emission extends from radio waves to GeV and sometimes TeV energies, with pulsations in different bands often arising from distinct regions[15]. Binary pulsars have enabled precise tests of various general relativistic effects, such as orbital period decay due to gravitational wave radiation [16, 17]. Additionally, due to their exceptional precision as cosmic clocks, pulsars offer insights into a wide

range of astrophysical phenomena, including the internal structure of neutron stars (NS) [18], the density of the interstellar medium[19], dark matter properties[20], and the gravitational wave background (GWB)[21].

There is expected to be a large population of neutron stars in the galactic center, on account of the high stellar densities, large molecular complexes, and the known population of young massive stars and stellar remnants[22–24]. However, detecting a pulsar in a close orbit around Sgr A* has proven challenging. The estimated number of ordinary neutron stars near Sgr A* with orbital periods below 100 years is approximately 1,000, while those with periods under 10 years are estimated to be around 100 [25]. Yet, alternative estimates based on non-detection suggest only about 90 ordinary pulsars in the central parsec [26]. More recent studies indicate there could be a large number of millisecond pulsars in the galactic center, with up to 10,000 of them possibly pointing their signals toward Earth [27]. Efforts to study the spacetime around Sgr A* also include near-infrared observations at distances of a few hundred Schwarzschild radii [28, 29] and detailed imaging of the event horizon using (sub-)millimeter telescopes with very-long baseline interferometry [5]. However, the expected high sensitivity of next-generation radio telescopes, like the Square Kilometer Array [30], the Five-hundred-meter Aperture Spherical Telescope [28], and the NASA Deep Space Network [31], could help overcome problems caused by high plasma density and strong magnetic fields in the galactic center.

Most of these studies mentioned above used the pulsar timing technique. It enables a highly accurate determination of the physical and orbital parameters of the neutron star [32, 33]. Pulsar timing involves carefully monitoring the times of arrival (TOAs) of radio signals or pulses released by pulsars that are observed on earth. The accuracy of TOA measurements for young pulsars near the Galactic Center (GC) with future telescopes will primarily be affected by three factors, each with distinct dependencies on observing frequency: the signal-to-noise ratio of the detected pulses, the intrinsic pulse phase jitter of the pulsar, and the changes in pulse shape due to interstellar scintillation [34, 35]. The pulsar research community currently relies on three primary data analysis packages for TOA analysis, that is,

TEMPO [36], TEMPO2 [37] and PINT [38]. The effectiveness of this method was first demonstrated with the binary system PSR B1913+16, where its orbital decay matched the predictions of General Relativity (GR) to within 0.5% accuracy [39]. The observed accumulated shift of its periastron was remarkably consistent with GR. Over time, pulsar timing has become a powerful tool for testing GR and exploring possible violations (e.g., [40, 41]) and as a result, many alternative gravity theories have been significantly constrained or even ruled out (see [42] for a recent review).

A study conducted by Damour and Deruelle (DD) [43] on a widely adopted timing model that includes all relativistic effects in the dynamics of a binary system up to the first post-Newtonian level has allowed the scientific community to perform self-consistent tests of gravity using the parametrized post-Keplerian (PPK) formalism. Their study presented the closed-form solution to the relativistic first post-Newtonian (PN) two-body problem, allowing for its direct application. The DD model represents a collection of pulsar timing formulas that use the DD framework to describe the binary orbit. This orbit can be characterized as either Keplerian or post-Keplerian. Additionally, a post-Newtonian spacetime description is typically employed to account for relativistic effects on the emission and travel times of photons emitted by the pulsar. This approach typically relies on the assumption of a weak gravitational field, characterized by $r_g/r \ll 1$, where $r_g = GM/c^2$ is the gravitational radius. For most binary systems with pulsars, r_g/r is usually around 10^{-6}. However, in the case of a pulsar closely orbiting a supermassive black hole, r_g/r can reach values as high as 10^{-2}. As a result, the validity of the post-Newtonian approximation, which relies on the weak-field assumption, must be carefully evaluated, particularly when the black hole is (nearly) aligned with the line of sight to the pulsar.

Hackmann and Dhani [10] derived an exact analytical formula for the propagation delay in a Schwarzschild spacetime. This paper highlights that for (nearly) edge-on orbits, the Shapiro delay with a lensing correction deviates significantly from the exact propagation delay. For Sgr A*, the maximum difference (superior conjunction) between the exact (analytical) formula and the sum of the single post-Newtonian delays reaches approximately $\sim 1\,\mathrm{s}$ for a pulsar orbiting at a distance of $r =$

$10^2 - 10^3 M$, with M, where M is the mass of Sgr A*. For inclined orbits, the difference decreases rapidly, to about $\sim 10^{-1}$ s for an orbit with the same radius but an inclination of $\pi/3$. Furthermore, Bilel and Hackmann [1] analyzed the effect of a comparison between an exact analytical solution for the frame-dragging delay and two post-Newtonian derivations. The results showed that post-Newtonian-based treatments overestimate the frame dragging effects on the lightlike signals, in particular around and after superior conjunction.

This work uses the pulsar timing model to investigate the time-frequency signal from a pulsar in orbit around a supermassive black hole. The black hole will induce strong relativistic effects on the pulsar's orbit and emission in an extreme mass ratio system. These relativistic effects within a supermassive black hole's gravitational field can impact pulsar signal arrival periods. Hence, it provides an opportunity to investigate the mass and spin of the black hole, thereby enhancing our understanding of pulsars and the supermassive black holes they orbit. In the weak-field limit, there are three key time delays: the Roemer delay, the Shapiro delay, and the Einstein delay. These delays are important in both the Solar System and pulsar binary systems. In a pulsar binary system, the Roemer delay occurs because the pulsar's orbit around its companion changes the distance between it and the observer. The basic effect on the signal emission is the Shapiro delay [44–47] which accounts for the modified velocity of light in the curved spacetime caused by the bending of light due to the gravitational field, such as that of the Sun in the Solar System or the pulsar's companion in a binary system. It is calculated using the weak-field approximation by solving the geodetic equations and is well understood up to the 2PN order. Corrections to account for lensing and geometric effects have also been developed [48]. The Einstein delay, on the other hand, arises from the difference between proper time and coordinate time, both at Earth (in the Solar System) and at the pulsar (in a binary system). This difference is due to the effects of the companion's gravity and time dilation. Lastly, the combined contribution of the Roemer and Shapiro delays is sometimes referred to as the "propagation delay."

Propagation delay as it relates to pulsar timing is the amount of time it takes for

pulsar signals to pass through the curved spacetime in the vicinity of the black hole as compared to the propagation time from a reference position[14]. With accurate timing measurements, researchers can gain insights into the dynamics of harsh environments detecting the aberrations brought on by the black hole's gravitational pull. The gravitational pull of a supermassive black hole can affect it, which plays a key role in pulsar timing. Time appears to move more slowly in larger gravitational fields due to time dilation caused by a strong gravitational field near the supermassive black hole. The measured pulse arrival times may be impacted if this influence causes a delay in the pulsar signals' reaching the observer. The primary focus of this thesis is to study pulsars in the framework of Schwarzschild spacetime. We derive the exact analytical solution for the propagation delay of the pulses and compare it with the corresponding post-Newtonian approximations. We derive the solution for the angle of emission.

The rest of this thesis covers the following: In Chapter two, we review the equations of motion for lightlike geodesics in Schwarzschild spacetime. We present an analytic solution for lightlike geodesics in Schwarzschild spacetime and determine the propagation time of a signal from a given spacetime position to an observer at infinity. Since pulsar timing detects only differences in delay along the pulsar's orbit, we measure the propagation delay rather than the absolute propagation time[10]. In chapter three, we review the weak field approximations of the propagation delay up to the second post-Newtonian order. Chapter 4 reviews the analytical approximations used in this work. We compare these approximations to the exact results and analyze their accuracy. We close the thesis with a summary and outlook for further study in chapter 5.

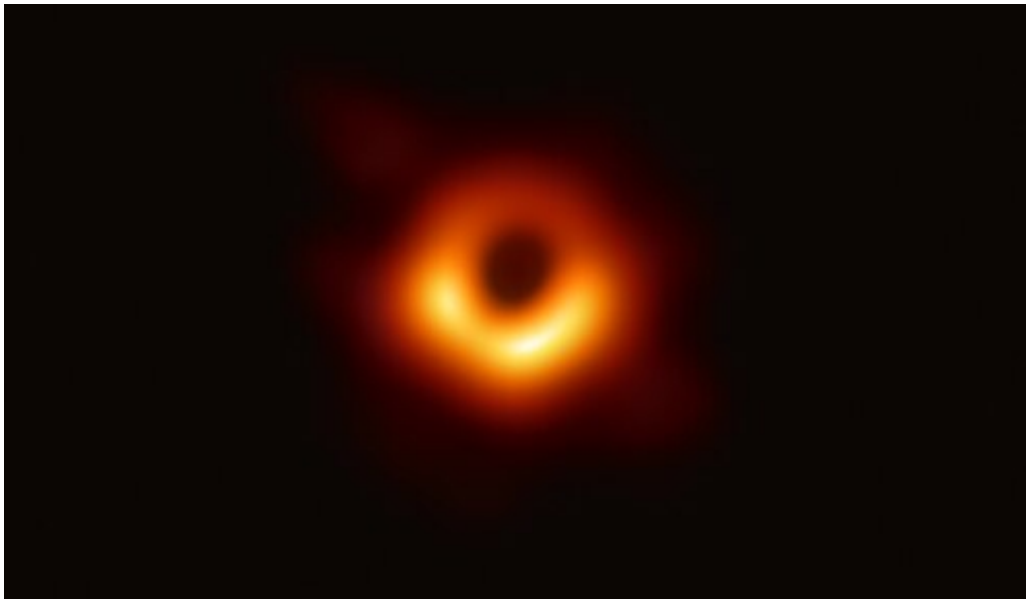

(a) The first direct image of a supermassive black hole in the core of Messier 87[49]

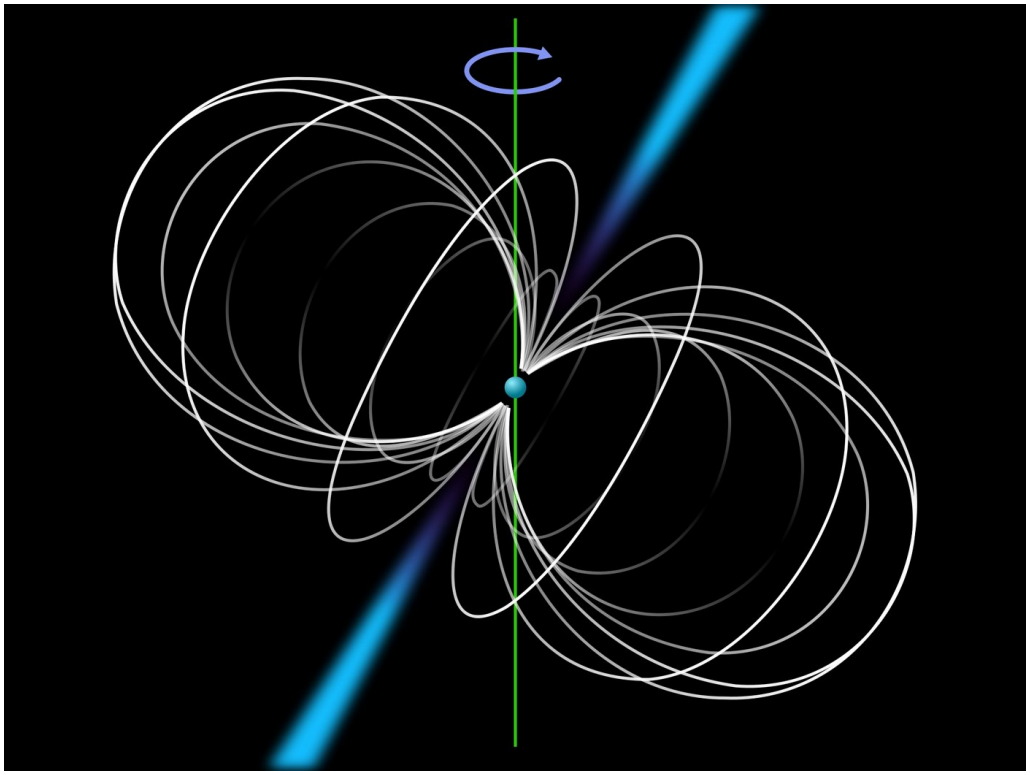

(a) Rotating pulsar, a rapidly spinning neutron star emitting beams of electromagnetic radiation.

Figure 1.1: Astrophysical Compact Objects

Chapter 2

Geodesic Motion in Schwarzschild Spacetime

In this work, we assume the full general relativity framework to describe both the motion of the pulsar around the supermassive black hole and the propagation of photons emitted from the pulsar to the observer in Schwarzschild metric. The most important tool is the geodesic equation. The lightlike geodesics are the worldlines of classical photons, that is, they tell how light propagates in the spacetime. The timelike geodesics are the worldlines of freely falling massive particles; e.g., we may think of planets moving in the gravitational field of the Sun.

2.1 The Schwarzschild metric

For static and spherically symmetric blackholes of mass, M, the Schwarzschild metric in spherical coordinates (t, r, θ, φ) is

$$ds^2 = -\left(1 - \frac{2m}{r}\right)(dx^0)^2 + \left(1 - \frac{2m}{r}\right)^{-1} dr^2 + r^2(d\theta^2 + \sin^2\theta d\varphi^2) \qquad (2.1)$$

where $m = GM/c^2$ is related to the mass M of the black hole. In this standard system, the coordinate variables are time t, radius r, polar angle θ, and azimuthal angle φ. The coordinate $x^0 = ct$ is associated with the coordinate time t, which due to asymptotic flatness is the proper time measured by an observer at infinity.

The Schwarzschild metric has three key properties:

- The Schwarzschild metric is *asymptotically flat*: For large values of r it approaches the Minkowski metric, which is, the metric of special relativity.
- The Schwarzschild metric is *static*: it is a timelike killing vector field that is orthogonal to hypersurfaces.

- The Schwarzschild metric is *spherically symmetric*: Every vector field that represents a rotation around a spatial axis is a Killing vector field. For a rotation about the z axis, the corresponding killing vector field is $\partial_\varphi = x\partial_y - y\partial_z$ (with (x, y, z) related to (r, θ, φ) by the usual transformation from spherical coordinates). For the remaining spatial axes, it can be demonstrated that (2.2) and (2.3) are killing vector fields.

$$K^{(x)} = y\partial_z - z\partial_y = -\sin\varphi\partial_\theta - \frac{\cos\theta}{\sin\theta}\cos\varphi\partial_\varphi \ , \tag{2.2}$$

$$K^{(y)} = z\partial_x - z\partial_y = \cos\varphi\partial_\theta - \frac{\cos\theta}{\sin\theta}\sin\varphi\partial_\varphi \ , \tag{2.3}$$

2.2 Geodesic motion

Photons travel along paths called null geodesics, which follow the geodesic equation.

$$\ddot{x}^\mu + \Gamma^\mu_{\nu\rho}\dot{x}^\nu\dot{x}^\rho = 0 \tag{2.4}$$

where x^μ is the position of a particle in spacetime with $\mu = 0, 1, 2, 3$. The term $\ddot{x}^\mu$ is the second derivative of position with respect to proper time (τ), representing the acceleration of the particle in spacetime. The Christoffel symbols are denoted as $\Gamma^\mu_{\nu\rho}$, representing the connection coefficients. We choose the orbital plane of the Schwarzschild spacetime geodesics as the equatorial plane $\theta = \frac{\pi}{2}$ due to the spherical symmetry. Hence, two constants of motion are related to the energy $\widetilde{E}$ and L, which is interpreted as the angular momentum per unit mass of the photon.

$$-E = -\widetilde{E}/c = g_{00}\frac{dx^0}{d\tau} = -\left(1 - \frac{2m}{r}\right)\frac{cdt}{d\tau} \tag{2.5}$$

$$L = g_{\varphi\varphi}\dot{\varphi} = r^2\frac{d\varphi}{d\tau} \tag{2.6}$$

The condition for null geodesics gives a third constant of motion.

$$g_{\mu\nu}\dot{x}^\mu\dot{x}^\nu = 0$$

From the Schwarzschild solution,

$$g_{\mu\nu}\dot{x}^{\mu}\dot{x}^{\nu} = -\left(1-\frac{r_s}{r}\right)c^2\dot{t}^2 + \frac{\dot{r}^2}{\left(1-\frac{r_s}{r}\right)} + r^2\dot{\varphi}^2 = \epsilon c^2 \tag{2.7}$$

where the dot denotes a derivative with respect to τ, where τ is an affine parameter or the proper time, and $\epsilon = 0$ for lightlike geodesics, $\epsilon = 1$ for timelike geodesics and ϵ = -1 for spacelike geodesics. Then,

$$\dot{r}^2 = -\epsilon c^2\left(1-\frac{r_s}{r}\right) + \left(1-\frac{r_s}{r}\right)^2 c^2\dot{t}^2 - r^2\dot{\varphi}^2\left(1-\frac{r_s}{r}\right) \tag{2.8}$$

$$= -\epsilon c^2\left(1-\frac{r_s}{r}\right) + \frac{E^2}{c^2} - \frac{L^2}{r^2}\left(1-\frac{r_s}{r}\right) \tag{2.9}$$

$$= \frac{E^2}{c^2} - \left(1-\frac{r_s}{r}\right) + \left(\epsilon c^2 + \frac{L^2}{r^2}\right) \tag{2.10}$$

$$= \frac{E^2}{c^2} - V_{eff}(r, L) \tag{2.11}$$

The term V_{eff}(r, L) is the effective potential for geodesic motion, and the derivation of an equation for r as a function of φ is seen below [50].

$$\left(\frac{dr}{d\varphi}\right)^2 = \frac{\dot{r}^2}{\dot{\varphi}^2} = \frac{E^2}{c^2L^2}r^4 - (r^2 - r_s r)\left(\frac{\epsilon c^2}{L^2}r^2 + 1\right) \tag{2.12}$$

$$= \frac{E^2 - \epsilon c^2}{c^2L^2}r^4 + \frac{\epsilon c^2 r_s}{L^2}r^3 - r^2 + r_s r \tag{2.13}$$

The equation of motion for lightlike geodesics in a Schwarzschild spacetime is given below with $\epsilon = 0$

$$\left(\frac{dr}{d\varphi}\right)^2 = \frac{E^2}{c^2L^2}r^4 - r^2 + r_s r = \frac{r^4}{d} - r^2 + r_s r =: R(r) \tag{2.14}$$

where $d = \frac{L^2c^2}{E^2}$ is called the impact parameter, φ is the photons angle and note that $\left(1-\frac{r_s}{r}\right)\frac{d}{r^2} < 1$ is a necessary condition for the existence of a physical solution. The

quartic polynomial $R(r)$ has four roots,

$$R(r) = \frac{1}{d}(r - r_0)(r - r_1)(r - r_2)(r - r_3) \tag{2.15}$$

with $r_1 < r_0 < r_2 < r_3$ if all roots are real, and $r_0 = 0$. The r_1 is always real and negative, whereas the two positive roots r_2 and r_3 have a double root for $d = d_{crit} = 27m^2$ at $r = 3m$. This implies that for $d > 27m^2$ we have either a flyby orbit, which comes from infinity turns at r_3 and returns to infinity, or a terminating bound orbit confined to the region $0 < r < r_2$. For $d < d_{crit}$, we have a terminating escape orbit which comes from infinity and falls into the singularity at $r = 0$. The critical value d_{crit} corresponds to the unstable circular orbit $r = 3m$, called the photon sphere. If an object shrinks to a radius smaller than $r = 3m$, an observer at the photon sphere would see their back by looking sideways due to strong gravitational lensing. Also, $d = 0$ corresponds to purely radial motion.

We transform equation (2.14) into an exact solution using the Jacobian elliptic function sn. A solution of the general differential equation below

$$\left(\frac{dy}{dx}\right)^2 = (1 - y^2)(1 - k^2y^2), y(0) = 0 \tag{2.16}$$

where k is a (real) parameter, is given by

$$x = \int_0^y \frac{d\tilde{y}}{\sqrt{(1 - y^2)(1 - k^2y^2)}} =: F(y, k) \tag{2.17}$$

The function F(y,k) is the (Jacobian) elliptic integral of the first kind. The inverse of F is the (Jacobian) elliptic function sn,

$$x = F(y, k) \Leftrightarrow y = sn(\varphi, k) \tag{2.18}$$

We reduce our problem in (2.16) by a general substitution of the form

$$r = \frac{\alpha n y^2 + \beta}{ny^2 + 1} \tag{2.19}$$

where α, β, and n are parameters that hold for $k^2 \geq 0$ and are chosen differently for different types of orbits. The rule is: when integrating between r_p (the finite radial turning point) and r_a (the maximal radial turning point), where r_p and r_a are zeros of $R(\varphi)$, we should set r_p to zero and r_a to one. This means that

$$r_p = \frac{\alpha n y^2 + \beta}{n y^2 + 1}|_{y=0} = \beta, \quad r_a = \frac{\alpha n + \beta}{n + 1} \tag{2.20}$$

Then α is chosen as a zero which is not r_p or r_a. Assume a flyby orbit. From our polynomial $R(r)$ with four real zeros $r_1 < 0 < r_2 < r_3$ with $r_p = r_3$ and $r_a = r_1$, we choose $r_p = r_3 = \beta$, and $\alpha = r_2$ leading to

$$r_1 \; = \; r_a \; = \; \frac{r_2 n + r_3}{n+1} \; \Leftrightarrow \; (n+1) r_1 \; = \; r_2 n + r_3 \qquad \Leftrightarrow \; n \; = \; -\frac{r_3 - r_1}{r_2 - r_1} \tag{2.21}$$

This results in the substitution

$$r = \frac{-r_2 \frac{r_3 - r_1}{r_2 - r_1} y^2 + r_3}{-\frac{r_3 - r_1}{r_2 - r_1} y^2 + 1} = \frac{r_2 y^2 (r_3 - r_1) - r_3 (r_2 - r_1)}{y^2 (r_3 - r_1) - (r_2 - r_1)} \tag{2.22}$$

Applying this substitution to our differential equation $R(r)$ with r(φ_0)= r_p, we find the result

$$\left(\frac{dy}{d\varphi} \right) = \frac{r_3 (r_2 - r_1)}{4d} [k^2 y^4 - (1 + k^2) y^2 + 1], \;\; y(\varphi_0) = 0 \tag{2.23}$$

where

$$k^2 = \frac{r_2 (r_3 - r_1)}{r_3 (r_2 - r_1)} \tag{2.24}$$

Then, the solution for lightlike geodesics in Schwarzschild spacetime is

$$y = sn \left(\sqrt{\frac{r_3 (r_2 - r_1)}{4d}} (\varphi - \varphi_0), \, k \right) \tag{2.25}$$

An example of lightlike geodesics is shown in the figure below

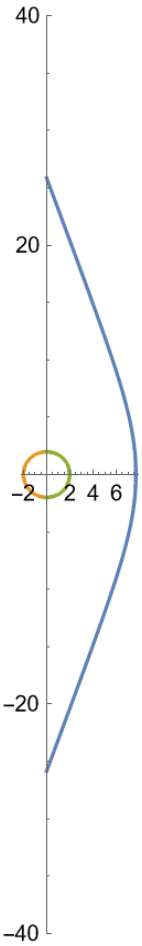

Figure 2.1: Lightlike geodesics in Schwarzschild spacetime. Flyby orbit with $d = 80$. Here, $G = c = M = 1$. The small circle indicates the Schwarzschild radius $r_s = 2$.

2.3 Propagation delay in Schwarzschild spacetime

In this work, we consider a pulsar orbiting a supermassive black hole. For this purpose, we revisit the geometrical framework introduced by [10], which forms the basis for this thesis. Because of the large difference in mass between the two objects, we can treat the pulsar as a test particle and assume the center of mass is at the center of the black hole. We set the origin of our coordinate system (X, Y, Z) with the black hole at the center so that the Z-axis aligns with the line of sight from the observer to the origin. In this case, the X-axis is defined by the ascending node of the pulsar's orbit relative to the plane of the sky. The inclination i of the pulsar's orbit is measured relative to the plane of the sky, which corresponds to the X-Y plane of our coordinate system (see Figure 2.2).

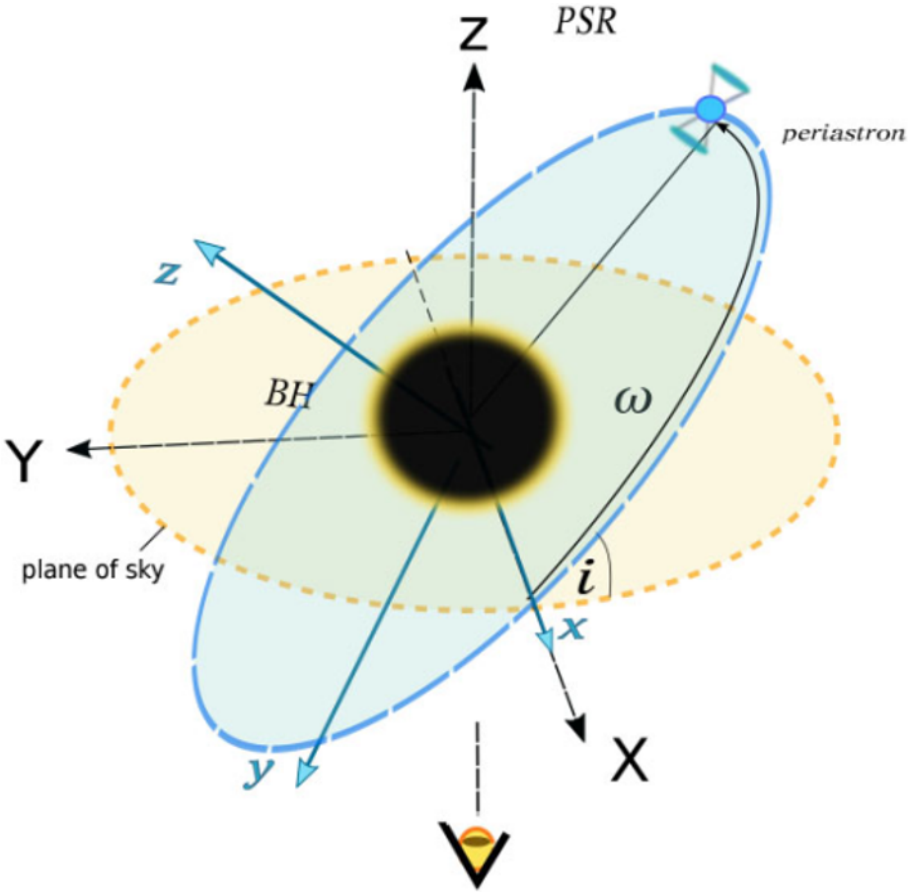

Figure 2.2: Orientation of the black hole–pulsar system in the sky with respect to an observer [1].

To calculate the time delay (2.30), we need the pulsar's radial distance r_e and its impact parameter d. The impact parameter d is derived from the pulsar's position (r_e, φ_e) in the plane shared by the pulsar, observer, and black hole, using a differential equation for the angle φ.

$$\left(\frac{dr}{d\varphi}\right)^2 = R(r), \quad r(\varphi_e) = r_e \tag{2.26}$$

$$\varphi_e = \int_\gamma \frac{dr}{\sqrt{R(r)}} = \int_{r_3}^{\infty} \frac{dr}{\sqrt{R(r)}} \pm \int_{r_3}^{r_e} \frac{dr}{\sqrt{R(r)}} \tag{2.27}$$

where $\varphi = 0$ was assumed at the observer position. A grid of impact parameters was used, and the corresponding angles of the photon's trajectory φ_e (for a fixed r_e) were calculated analytically using the Jacobian elliptic integrals explained in Appendix A. We chose values for r_e, r_o, and calculated Y_e and Y_o for respective orbit types where Y_e and Y_o are normalized values that represent the relative position

of r_e and r_o, that is, the point of emission and some reference point of observation. We analytically derived the formula for $R(r)$ in terms of φ_e using the Jacobi elliptic integral, as detailed in Appendix A.

$$R(\varphi) = \frac{r_2(r_1 - r_3)\ sn\left(\frac{1}{2}\sqrt{d(r_1 - r_2)r_3}\ \varphi \middle| k\right)^2 + r_3(r_2 - r_1)}{(r_1 - r_3)\ sn\left(\frac{1}{2}\sqrt{d(r_1 - r_2)r_3}\ \varphi \middle| k\right)^2 - r_1 + r_2} \tag{2.28}$$

A photon following its geodesic from an emission point, E, to an observer at infinity, has an infinite travel time value (see Figure 2.3). To have a finite quantity, we calculate the relative travel time delay between a photon emitted at an assumed reference point along the pulsar trajectory with the corresponding impact parameter d_{ref}. Since we are interested in the arrival times of photons as measured by an observer at infinity, in the Schwarzschild metric we have

$$c(t_a - t_e) = \int_\gamma \frac{r^2 dr}{d\left(1 - \frac{r_s}{r}\right)\sqrt{R(r)}} \tag{2.29}$$

$$= \int_{r_3}^{\infty} \frac{r^2 dr}{d\left(1 - \frac{r_s}{r}\right)\sqrt{R(r)}} \pm \int_{r_3}^{r_e} \frac{r^2 dr}{d\left(1 - \frac{r_s}{r}\right)\sqrt{R(r)}} \tag{2.30}$$

where t_e corresponds to the time of emission at the radius of emission r_e and t_a is the time of arrival at r = ∞. The integration path γ begins at r_e and then moves to the turning point r_3 for a flyby orbit, which first decreases in radius or moves directly to $r = \infty$. This means that if r is always increasing, we use the minus sign in (2.30); otherwise, we use the plus sign. Also, when $d < d_{crit}$, r_3 becomes one of two complex conjugate roots, but the full expression still turns out to be real[51]. The integral in (2.30) can be solved exactly in terms of elliptic integrals and the details of the calculation can be found in Appendix A. The result is

$$\frac{c}{m}(t_a - t_e) = T(\infty, d) \pm T(r_e, d) \tag{2.31}$$

with $T(r,\ d)$ given by

$$
\begin{aligned}
T(r,d) = \frac{2}{\sqrt{r_3(r_2-r_1)}}\Bigg[& \left(\frac{r_2^3}{r_2-2} + \frac{1}{2}(r_3-r_2)(r_2-r_1+4)\right) F(x,k) \\
& - \frac{1}{2}r_3(r_2-r_1)E(x,k) - 2(r_3-r_2)\Pi\left(x, \frac{k^2}{c_1}, k\right) \\
& - \frac{8(r_3-r_2)}{(r_3-2)(r_2-2)}\Pi(x,c_2,k)\Bigg] + \frac{d\sqrt{R(r)}}{(r-r_2)} \\
& + 2\ln\left(\frac{\sqrt{r(r-r_1)} + \sqrt{(r-r_3)(r-r_2)}}{\sqrt{r(r-r_1)} - \sqrt{(r-r_3)(r-r_2)}}\right),
\end{aligned}
\tag{2.32}
$$

refer to (A15). Here, x is related to r by (A2), k is defined in (2.24), and c_1, c_2 are given in (A6). The zeros of $R(r)$, namely r_0, r_1, r_2, r_3, are the same as in (2.15). All quantities in equation (2.32) are made dimensionless, which is why the factor c/m appears in (2.31). The Jacobian elliptic integrals F, E, and Π are defined in (A8)–(A10). The time to reach infinity diverges. The normalized impact parameter d must be determined from the emission position. In numerical integration, it is not straightforward to isolate and cancel the diverging parts of the integral relative to a reference point. In the analytical solution (2.32), the divergence comes from the last two terms, which involve $r + 2\ln(r)$, as shown in (A20) and (A21). These diverging terms, independent of the impact parameter d, will cancel when considering the travel time delay with respect to a reference point using their Taylor expansions[10].

The propagation time delay is given as the difference between the time delay of a signal from the actual position of the pulsar and some reference point.

$$
\Delta t_{ex}(r_e, \varphi_e) = (t_a - t_e)(r_e, \varphi_e) - (t_a - t_e)(r_{ref}, \varphi_{ref}) \tag{2.33}
$$

$$
= \frac{m}{c}[T(\infty, d_e) \pm T(r_e, d_e)] - \frac{m}{c}[T(\infty, d_{ref}) \pm T(r_{ref}, d_{ref})] \tag{2.34}
$$

where $d_e = d(r_e, \varphi_e)$ *and* $d_{ref} = d(r_{ref}, \varphi_{ref})$

The finite difference between the arrival times of signals from the pulsar as it orbits the central supermassive black hole is only considered. However, the diverging terms in T(∞, d_e) and T(∞,d_{ref}) directly cancel each other, as in (A15).

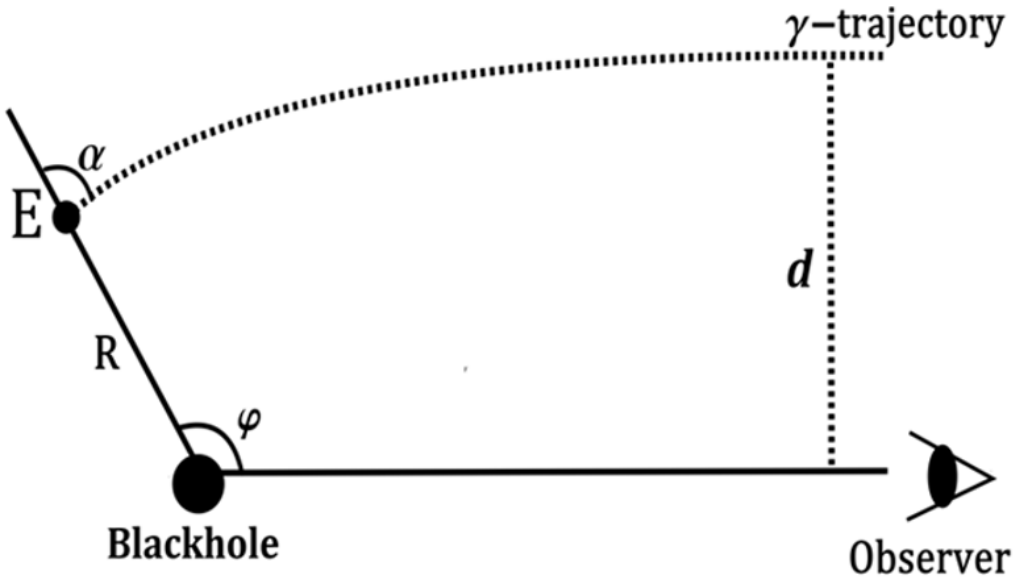

Figure 2.3: Example of photon trajectory
The photon is emitted at **E** with radius **R**, the angle of the photon trajectory φ, $\boldsymbol{\alpha}$ is the angle between the radial direction and the initial direction needed for the photon to reach the observer at infinity parallel to the line of sight with the corresponding impact parameter $\boldsymbol{d}$.

Chapter 3

The propagation delay in the weak field regime

In the weak-field approximation, (where $\frac{v}{c} \sim \frac{m}{r} \ll 1$ with the velocity v and the radius r of the particle), the propagation time delay consists of the Roemer delay, which is the time it takes for the signal to travel across the orbit, and the Shapiro delay (calculated to the first post-Newtonian order), which arises from variations in the three-velocity of light in the gravitational field. Typically, pulsar timing models account for only these two effects. Other effects, such as the geometric delay Δ_{geo}, account for the signal's curved path through spacetime, and a second-order Shapiro delay comes into play at higher precision (second post-Newtonian order).

3.1 The weak field metric

We recall the assumptions that lead to the Newtonian limit, which include[50]:

(N1) The gravitational field is weak, meaning it deviates only slightly from the Minkowski metric ($\eta_{\mu\nu}$):

$$g_{\mu\nu} = \eta_{\mu\nu} + h_{\mu\nu} \tag{3.1}$$

where $h_{\mu\nu}$ is so small that we need only consider terms of the first order in $h_{\mu\nu}$ and $\partial_\rho h_{\mu\nu}$.

(N2) The gravitational field is time-independent:

$$\partial_0 h_{\mu\nu} = 0 \tag{3.2}$$

That is, the gravitational field is assumed to be constant over time.

(N3) The velocity of particles is small, that is,

$$\left|\dot{x}^i\right| \ll \left|\dot{x}^0\right| \quad \Rightarrow \quad \left|\frac{\dot{x}^i}{\dot{x}^0}\right| = \left|\frac{v^i}{c}\right| \ll 1 \tag{3.3}$$

where $v^i = \frac{dx^i}{dt}$ denotes the three-velocity. The equation describes a regime where the particle's velocity is non-relativistic, meaning it is much smaller than the speed of light ($v \ll c$). In this approximation, the spatial components of the velocity are much smaller than the time component of the 4-velocity, so relativistic effects (such as time dilation and length contraction) are negligible.

(N4) The mass is static, and only the mass density (μ) generates the gravitational field:

$$T_{00} = c^2\mu, \quad T_{0i} = 0, \quad T_{ik} = 0 \tag{3.4}$$

where $T_{00} = c^2\mu$ represents the energy density, $T_{0i} = 0$ corresponds to the momentum density (which is zero because the mass is static and has no motion), and $T_{ik} = 0$ corresponds to the stress components, such as pressure or shear forces, which are negligible in this approximation.

For the Schwarzschild metric (2.1), the first condition is satisfied if r is large compared to r_s. The second and fourth conditions are satisfied everywhere, and the third condition gives no restriction on the metric. The equation below

$$g_{00} = -\left(1 + \frac{2\phi}{c^2}\right) \tag{3.5}$$

holds in the Newtonian limit, and is valid for the Schwarzschild metric when r is sufficiently large. Hence, with the spherically symmetric Newtonian field $\phi(r) = -\frac{GM}{r}$, we find

$$-\left(1 - \frac{r_s}{r}\right) = -\left(1 - \frac{2GM}{c^2 r}\right) \implies r_s = \frac{2GM}{c^2} \tag{3.6}$$

where G = c = 1. This demonstrates that the mass M of the central body determines the integration constant r_s. M can be measured based on Newtonian theory at a sufficiently large distance from the center. $\boldsymbol{r_s}$ is called the Schwarzschild radius or the gravitational radius of the central body. For positive M, the Schwarzschild radius

r_s is positive. If the radius R of the central body is smaller than the Schwarzschild radius, $R < r_s$, a zero occurs in the denominator of the Schwarzschild metric (2.1). For normal celestial bodies, we have $R \gg r_s$; ensuring that the Schwarzschild metric remains regular throughout its domain of validity. For the Sun, $r_s \approx 3$km, and for the Earth, $r_s \approx 1$cm. In harmonic coordinates, the Schwarzschild metric can be approximated in the weak field regime up to the second post-Newtonian order as follows [47]:

$$ds^2 = -\left(1 - \frac{2m}{r} + \frac{2m^2}{r^2}\right)c^2dt^2 + \frac{m^2x^ix^j}{r^2}dx^idx^j + \delta_{ij}\left(1 + \frac{2m}{r} + \frac{m^2}{r^2}\right)dx^idx^j \tag{3.7}$$

where terms of v^6/c^6 are neglected, and $r = |\vec{x}|$ is used. This simplifies the first post-Newtonian order as:

$$ds^2 = -\left(1 + \frac{2\Phi}{c^2}\right)c^2dt^2 + \left(1 - \frac{2\Phi}{c^2}\right)(d\vec{x}), \tag{3.8}$$

by neglecting terms of order v^3/c^3 and using $(d\vec{x})^2 = dx^2 + dy^2 + dz^2$, where $\Phi(\vec{x}) = -\frac{GM}{r}$ represents the Newtonian gravitational potential of the supermassive black hole. The normalization condition for null geodesics $g_{\mu\nu}dx^\mu dx^\nu = 0$ can be expressed as

$$cdt = \left(1 - \frac{2\Phi}{c^2}\right)^{\frac{1}{2}}\left(1 + \frac{2\Phi}{c^2}\right)^{-\frac{1}{2}}d\vec{x} \approx \left(1 - \frac{2\Phi}{c^2}\right)d\vec{x}, \tag{3.9}$$

which simplifies to (3.10) by integration.

$$c(t_a - t_e) = \int_{\overrightarrow{r_e}}^{\overrightarrow{r_a}}\left(1 - \frac{2\Phi(\vec{x})}{c^2}\right)d\vec{x} \tag{3.10}$$

Here, $\overrightarrow{r_e}$ and $\overrightarrow{r_a}$ represent the points of emission and arrival at times t_e and t_a, respectively. In the first-order approximation, the signal is assumed to travel in a straight line from the pulsar to the observer.

$$\vec{x}(t) = r_e + \frac{t - t_e}{t_a - t_e}(r_a - r_e). \tag{3.11}$$

The integral in (3.10) then reduces to

$$c(t_a - t_e) = |r_a - r_e| + \frac{2GM}{c} \int_{t_e}^{t_a} \frac{dt}{|x(t)|} \tag{3.12}$$

$$= |\overrightarrow{r_a} - \overrightarrow{r_e}| + \frac{2GM(t_a - t_e)}{c|\overrightarrow{r_a} - \overrightarrow{r_e}|} \times \ln\left(\frac{|\overrightarrow{r_e}(\overrightarrow{r_a} - \overrightarrow{r_e})| + |\overrightarrow{r_a} - \overrightarrow{r_e}|^2 + |\overrightarrow{r_a}||\overrightarrow{r_a} - \overrightarrow{r_e}|}{|\overrightarrow{r_e}(\overrightarrow{r_a} - \overrightarrow{r_e})| + |\overrightarrow{r_e}||\overrightarrow{r_a} - \overrightarrow{r_e}|}\right) \tag{3.13}$$

Assuming $c(t_a - t_e) \approx |r_a - r_e|$ and $|r_a| \approx |r_e|$, we obtain

$$c(t_a - t_e) = |\overrightarrow{r_a} - \overrightarrow{r_e}| + \frac{2GM}{c^2} \ln\left(\frac{2|\overrightarrow{r_a}|}{|\overrightarrow{r_e}| + |\overrightarrow{r_e}| \cdot \overrightarrow{n}}\right). \tag{3.14}$$

where $\overrightarrow{n} = \overrightarrow{r_a}/|\overrightarrow{r_a}|$ is the unit vector pointing towards the observer. We can neglect all constant contributions to the time delay for pulsar timing purposes since they only result in a constant shift that cannot be detected. The first term in expression (3.14) corresponds to the **Roemer delay**. Its time-varying component represents the time of flight across the orbit and can be approximated as $-\overrightarrow{r_e} \cdot \overrightarrow{n}$, with $-\overrightarrow{r_e} \cdot \overrightarrow{n} = -r \sin i \sin(\omega + \phi)$.

3.2 The Roemer and the Shapiro delay

Based on the weak-field propagation delay in pulsar timing derived Blandford and Teukolsky [45], the Roemer delay is expressed as:

$$\Delta t_R = \frac{a(1 - e^2) \sin i \sin(\omega + \phi)}{c(1 + e \cos \phi)}, \tag{3.15}$$

where i is the inclination of the orbital plane with respect to the plane of sky, a is the semi-major axis, ω is the argument of periapsis, ϕ is the argument of the pulsar's position, and e is the eccentricity of the orbit. The Shapiro delay is

$$\Delta t_S = \frac{2GM}{c^3} \ln\left[\frac{1 + e \cos \phi}{1 - \sin i \sin(\omega + \phi)}\right]. \tag{3.16}$$

The Roemer delay vanishes at $\phi = -\omega$, while the Shapiro delay vanishes at

$$\phi = \arctan\left[\frac{-e - \sin i \sin\omega}{\sin i \cos\omega}\right]. \tag{3.17}$$

For circular orbits where $e = 0$, we also have $\phi = -\omega$, representing the ascending node. The reference point is where the time delay is zero. The formula (3.16) diverges for edge-on trajectories with $i = \frac{\pi}{2}$ at superior conjunction, when $\omega + \phi = \frac{\pi}{2}$. This happens because light passing through a central object encounters an infinitely deep gravitational potential. To fix this, we use the lensing path introduced by Lai and Rafikov [52] and updated by Schneider [53]. The generalized result is:

$$\Delta t_{S,I} = \frac{2GM}{c^3} \ln\left[\frac{a(1-e^2)}{\sqrt{|\vec{r_e}\cdot\vec{n}|^2 + |\vec{r\pm}|^2} - \vec{r_e}\cdot\vec{n}}\right] \tag{3.18}$$

where r± is the approximate position of the image of the source in the plane of the sky,

$$r_\pm = r_s\left(1 \pm \sqrt{1 + \frac{4R_E^2}{|r_s|^2}}\right), \tag{3.19}$$

and $\vec{r_s}$ is the projection of $\vec{r_e}$ onto the sky plane,

$$\vec{r_s} = \vec{r_e}\sqrt{1 - \sin^2 i \sin^2(\omega\phi)}. \tag{3.20}$$

Here, R_E denotes the Einstein radius, which is approximately given by $R_E^2 = \frac{4GM}{c^2}\sin i$ at superior conjunction, while the magnitude of the emitter's position vector is $\vec{r_e} = a(1-e^2)/(1 + e\sin\omega)$.

3.3 The Geometric Delay

The geometric delay is the extra time a light ray takes to travel along a curved path within the gravitational potential of the black hole, compared to a direct straight-line path. This delay is only considered when the pulsar is on the far side of its orbit around the black hole. The geometric delay is largest when the pulsar is

directly behind the black hole. To first-order approximation, the light ray's path is approximated as a straight line from the emission point to the closest approach to the black hole and then from there to the observer. The delay is calculated as the difference between the length of this curved path and the direct straight-line path from the pulsar to the observer.

La Rafikov gave the expressions for the geometric delay. This delay to the first order is given by [52]

$$\Delta t_{\text{geo}} = \frac{2GM}{c^3}\left[\frac{|r_\pm - r_s|}{R_E}\right]^2. \tag{3.21}$$

If R_E is much larger than $|r_s|$, then $|r_\pm - r_s| \to R_E$, causing the two images to form an Einstein ring. On the other hand, when $|r_s| \gg R_E$, we get $|r_+ - r_s| \to R_E^2/|r_s|$ and $|r_- - r_s| \to |r_s|$, with the '-' image being very faint, making its contribution negligible.

3.3.1 The second-order Shapiro delay

The second-order Shapiro delay, as derived by [47], can be written in the second post-Newtonian order as:

$$\Delta t_{2PN} = \frac{GM}{c^3 r}\left(-4\left(\frac{1}{1+\cos\varphi_e}\right) + \frac{\cos\varphi_e}{4} + \frac{15\varphi_e}{4}\sin\varphi_e\right),$$

where φ_e is the angle between the emission position vector $\vec{r_e}$ and the receiver position vector $\vec{r_a}$, and $r = a(1-e^2)/1 + e\cos\varphi$. From the expression, we observe that at inferior conjunction ($\varphi_e = 0$), the last term remains finite, while at superior conjunction ($\varphi_e = \pi$), the first term diverges.

Chapter 4

Analytical Approximations in Schwarzschild Spacetime: Results and Discussion

In this section, we explore three analytical approximations that have been widely used in scientific studies involving the impact parameter d and the time of flight of signals. These approximations have proven useful in various contexts, such as calculating the bending of light around massive objects. However, they have not yet been applied to studying propagation delays in pulsar timing. Although these methods may provide reasonable accuracy for some calculations, their reliability in predicting time delays remains uncertain. The precision of pulsar timing measurements is important for testing general relativity and detecting relativistic effects, such as gravitational waves or variations in spacetime curvature. If these approximations introduce errors in time delay calculations, they could limit the accuracy of analytical timing models when compared to more precise post-Newtonian approaches. Hence, to determine whether these approximations work well for pulsar timing, we need to compare them with more precise numerical methods. Further analysis is needed to assess their limitations and identify any potential corrections that could improve their accuracy.

Beloborodov presented a simple formula for the bending angle that replaces the elliptic integral with high accuracy at radii $R \geq 2r_g$. The bending effects are well understood and described accurately, as long as stars with $R > 2r_g$ are considered [54]. We considered the approximate cosine relation in the Schwarzschild metric, which was proposed, and its effect is described by computing the angle α with respect to the radius along a photon trajectory. According to Beloborodov, Equation (4.1) shows high accuracy, which is a key feature of the Schwarzschild spacetime.

$$1 - \cos\alpha = (1 - \cos\varphi)\left(1 - \frac{r_s}{R}\right) \tag{4.1}$$

where $r_s = 2GM/c^2$ is the Schwarzschild radius of the gravitating spherical object of mass M, α is the emission angle (between the emitted photon and the local radial direction), φ is the angle of the photon trajectory and R is the point of emission (see 2.3). The standard form of this emission angle α is shown below

$$\sin\alpha = \frac{b}{R}\sqrt{1-\frac{r_g}{R}} \tag{4.2}$$

where b is the impact parameter.

Poutanen and Beloborodov [55] proposed an approximate expression obtained through a second-order expansion in y, as shown below

$$\frac{1-\cos\alpha}{1-u} = y\left(1+\frac{u^2}{112}y^2\right) \tag{4.3}$$

where $y = 1-\cos\varphi$, u $= r_s$/R, and the other symbols as aforementioned. This approximation is accurate to within 20% for most emission angles and compactness values. However, in extreme cases, such as when $R = 2r_s$ and bending angles are large (leading to longer delays), the error increases to about 35%. Since time delays have only a small effect, equation (4.3) is generally sufficient for most calculations [55].

Another formula of interest was proposed by La Placa et al. [56]. An approximate equation which holds for φ between 0 and π, considered up to the maximum, α(r, $\varphi = \pi$)) and keeps $\delta\alpha/\alpha$ at 1% throughout:

$$1-\cos\alpha \approx (1-\cos\varphi)\left(1-\frac{2r_s}{r}\right)\left[1+k_1\frac{2r_s}{r}\left(1-\cos(\varphi-k_2)\right)^{k_3}\right] \tag{4.4}$$

where $k_1 = 0.1416, \quad k_2 = 1.196, \quad k_3 = 2.726$. The values of the k-parameters were found by fitting the relationship between α and φ to the geodesics calculated for various radii between 6 and 100 r_s, and by adjusting the parameters for $r = 10r_s$.

Recall in Section (2.3) were we calculated the exact propagation delay and also computed the emission angle φ as a function of the impact parameter d (see Figure 4.2 for illustration). We used the three approximations introduced in this chapter to derive an approximate relationship between d and φ for photon signals reaching an

observer at infinity. For this analysis, we consider a pulsar in circular orbit around a blackhole, emitting signals from fixed radial distances r_e. We examined $r_e = 10m$, $100m$, and $1000m$, while keeping r_o (the point of observation) constant. To determine the maximum impact parameter ($d_{\max}$), we used the polynomial function $R(r)$, as presented in Equation (2.14). The value of $d_{\max}$ corresponds to the point where the photon's trajectory (flyby orbit) touches the pulsar's orbit, i.e., where $r_p = r_e$, with r_p being the closest approach to the black hole. Thus, we have $d_{\max} = \frac{r_e^3}{r_e - 2}$ which defines the boundary where the direct flyby is equal to the indirect flyby. Furthermore, to assess the accuracy of the approximations, we calculated the difference between the exact and approximate values of impact d for:

- The terminating escape orbit - $d < d_{\max}$, in which the photon comes from infinity and falls into the singularity at $r = 0$.
- The flyby orbit (direct and indirect) - $d > 27m^2$, in which the photon comes from infinity turns at r_3 and returns to infinity, or a terminating bound orbit confined to the region $0 < r < r_2$.

Next, we show plots comparing these approximations at different emission radii to evaluate their accuracy. Figure 4.3 shows the difference between the exact impact parameter$d$ and the approximated d derived from the approximation by Beloborodov (4.1) for $r = 10m$. The plot shows that this approximation works well for the terminating escape and the direct flyby orbits for φ between 0 and $\approx 5\pi/8$. However, as expected, it does not behave well when the pulsar is behind the black hole, as seen in the indirect case, particularly between $3\pi/4$ to $\approx \pi$. This indicates that the approximation should not be used in this region, as it produces errors. Similar trends were observed when higher values of r were considered for the circular pulsar orbit.

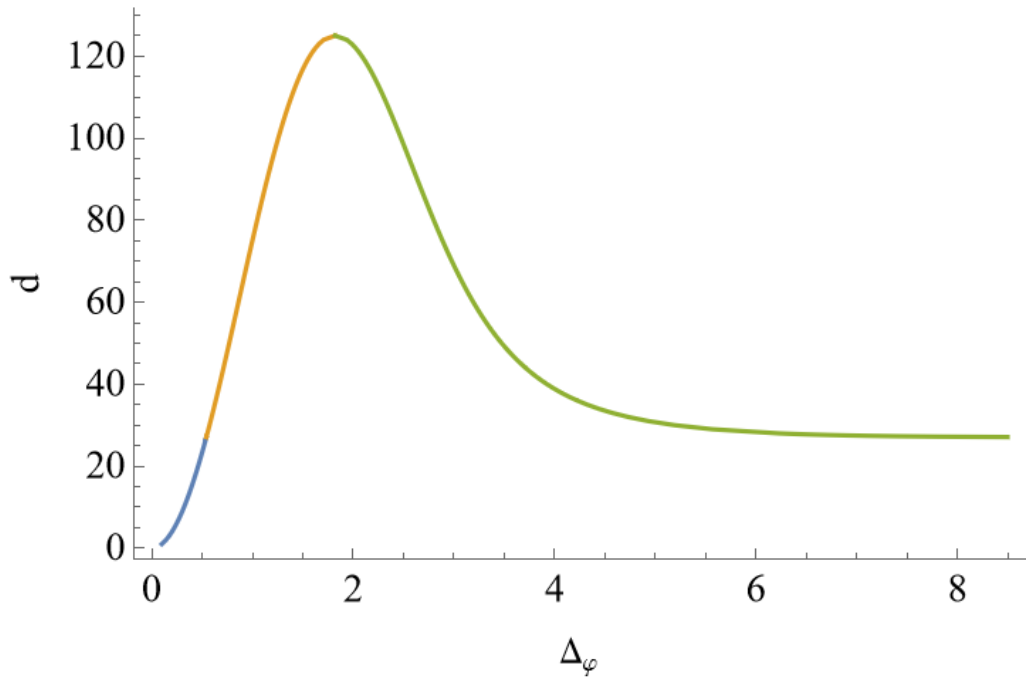

Figure 4.1: Plot of change in angle (Δ_φ) as a function of impact parameter d for circular pulsar orbit with Schwarzschild radial coordinate $r = 10\,m$ with $d_{max} = 125$. The blue solid line represents the terminating escape orbit, the orange solid line represents the direct fly orbit and the green represents indirect flyby orbit.

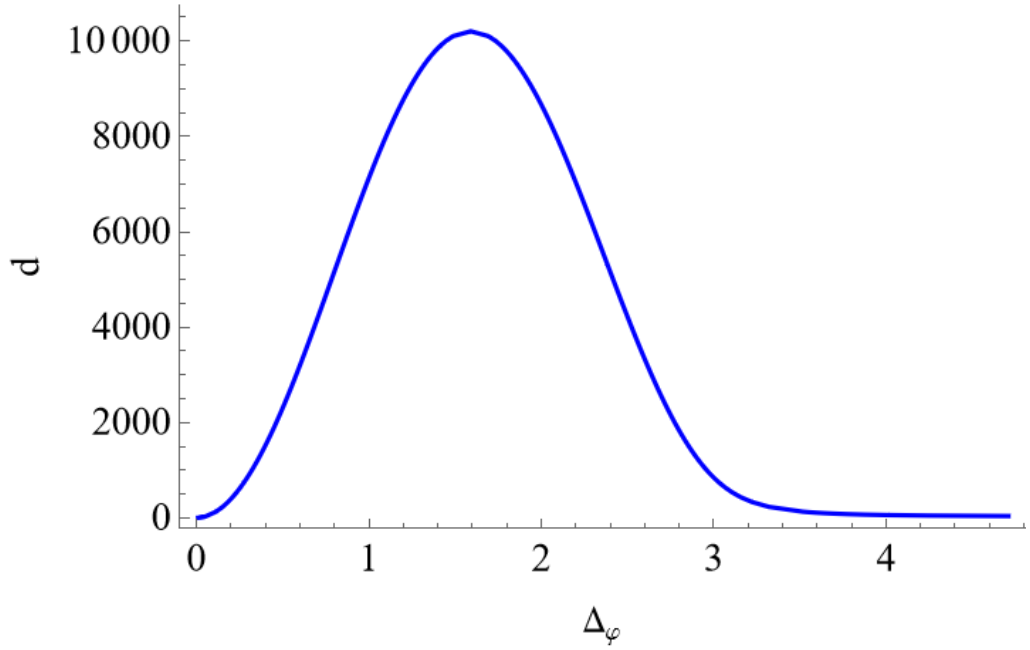

Figure 4.2: Plot of change in angle (Δ_φ) as a function of impact parameter d for circular pulsar orbit with Schwarzschild radial coordinate $r = 100\,m$ with $d_{max} = 500000/49$. The blue solid line represents the combined output for terminating escape, direct flyby and indirect flyby orbit.

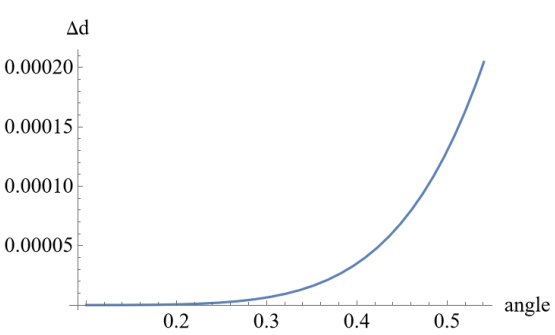

(a) Terminating escape $r = 10$m

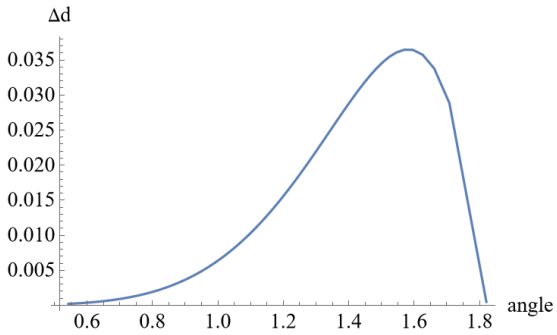

(b) Direct flyby $r = 10$m

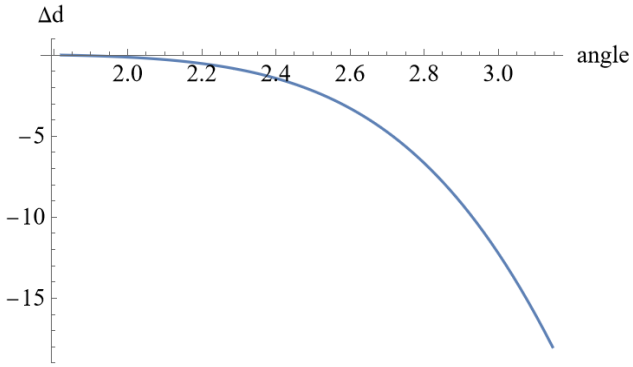

(c) Indirect flyby $r = 10$m

Figure 4.3: Difference between the exact impact parameter d and the approximated d derived from the approximation by Beloborodov (4.1) for $r = 10m$.

The difference between the exact impact parameter$d$ and the approximated d derived from the approximation by Poutanen & Beloborodov (4.1) for $r = 100m$ was explored in Figure 4.4. In the case of the terminating escape orbit, we observe some irregularities such that, although the difference remains relatively small, it is inconsistent and does not follow a clear increasing or decreasing trend. The approximation behaves well for the direct flyby orbit for φ between 0.05 and $\approx 5\pi/8$ but again the approximation fails when the pulsar is behind the black hole, as observed in the indirect case where φ is between $3\pi/4$ and $\approx \pi$. This indicates that the approximation should not be used in this region, as it produces errors, including when other values for r are considered.

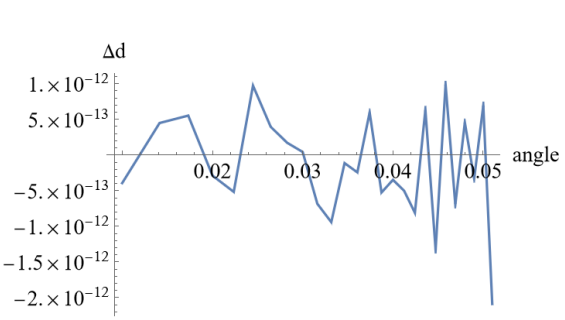

(a) Terminating escape $r = 100$m

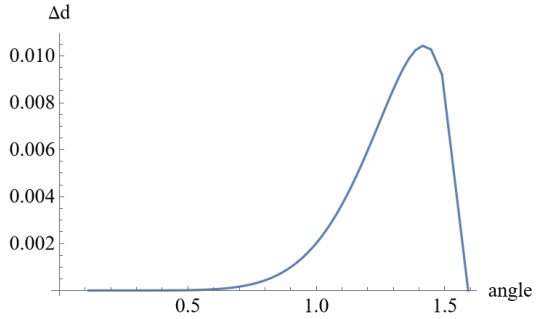

(b) Direct flyby $r = 100$m

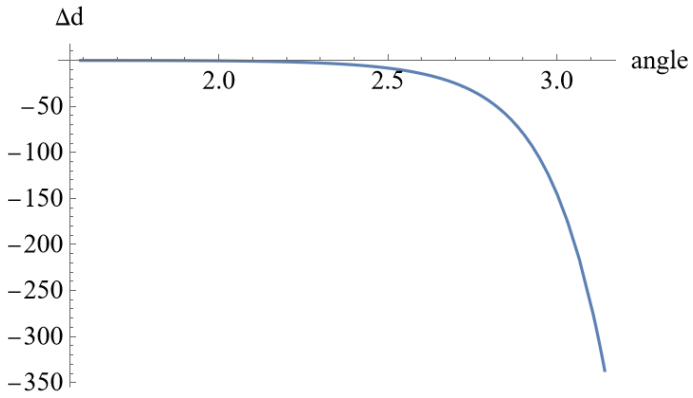

(c) Indirect flyby $r = 100$m

Figure 4.4: Difference between the exact impact parameter d and the approximated d derived from the approximation by Poutanen & Beloborodov (4.1) for $r = 100m$.

Figure (4.5) shows the difference in impact parameter d between the exact and approximated values based on the approximation by La Placa et al.(4.3) for $r = 1000m$. In this case, the approximation works well for the terminating escape when φ is between 0.05 and 0.0005, although the difference shows a negative trend. The approximation also works reasonably well for the direct flyby orbits and the indirect case - where the pulsar is behind the black hole, particularly between $3\pi/4$ and $\approx \pi$. However, the differences between the exact and approximated values are quite high. Hence, while the approximation is recommended for use in this region, further investigation is needed to asses the accuracy. Similar results were found for other values of r in the circular pulsar orbit.

It is worth mentioning that this analysis, which compares the exact and approximate impact parameters d, helps us assess how well our approximations work in different situations involving the gravitational pull of the black hole. This comparison allows us to evaluate the reliability of the models used for understanding

how light behaves around black holes especially in pulsar timing, where accurate time delay predictions are crucial. Each of these cases provides valuable insight into the limits of the approximations, helping us improve the models and make more accurate predictions in the study of black holes.

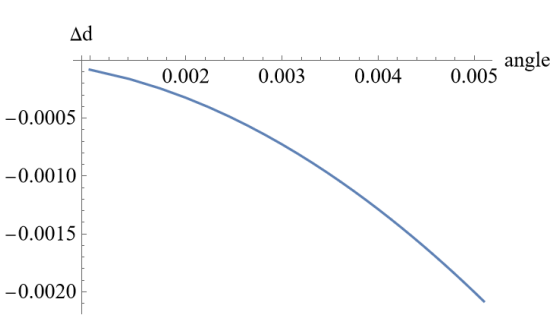

(a) Terminating escape $r = 1000$m

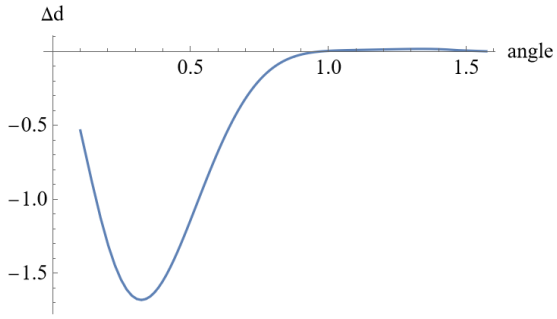

(b) Direct flyby $r = 1000$m

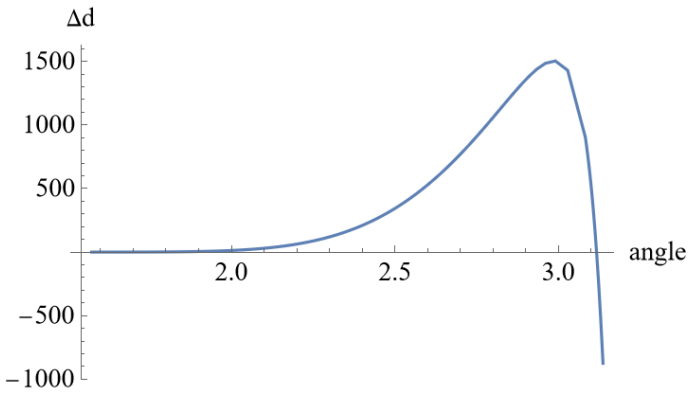

(c) Indirect flyby $r = 1000$m

Figure 4.5: Difference in Impact Parameter: Exact d - Approximated d obtained from the approximation by La Placa et al. for $r = 1000m$.

4.1 Results and Discussion

In this section, we present both the exact relativistic propagation time delay derived in this work and the approximated propagation time delays calculated using the three analytical approximations discussed earlier. The goal is to compare these results to assess how accurate each approximation is for a pulsar orbiting a supermassive black hole with a mass of M $= 4 \times 10^6 M_\odot$, where $m_{Sun} = GM_{Sun}/c^2 = 1476m$. The results of the propagation time delay are presented in dimensionless form by dividing

the time in seconds by $GM/c^3 \approx 19.7\,\mathrm{s}$.

Figures 4.6 - 4.8, show the differences between the exact propagation delay Δ_{ex} in the Schwarzschild spacetime and the delays calculated using the analytical approximations presented in this chapter for various values of the Schwarzschild radial coordinate, $r = 10m$, $100m$, and $1000m$. To explore the results change, we increased the Schwarzschild radial coordinate of the edge-on orbit for every line-style by a factor of ten. We assumed that the pulsar's orbit that lies in the same plane as the observer, such that the observer views the orbit edge-on. The relativistic effects are expected to be strongest when the pulsar orbit aligns with a superior conjunction, where the pulsar lies directly behind the black hole along the observer's line of sight. Figure 4.6 shows that the first-order approximation by Beloborodov starts to deviate from the exact results around $\varphi = 5\pi/8$. Therefore, this approximation may not be accurate enough in regions where φ approaches π, where the trajectory is highly bent. This suggests that a modified formula might be more suitable for such geometries.

We also observed similar results with the second-order approximation by Poutanen & Beloborodov [55], which showed similar behaviour to the first-order approximation. To clearly illustrate our results and for better comparison, we chose a higher radius for r, increasing r by a factor of 10, and plotted the results in Figure 4.7. For $r = 100m$, the calculated delays for both approximations (4.1) and (4.3) behave well and follow the exact reference closely up to $\varphi = 3\pi/4$, but they still deviate significantly from the exact delay at this point. Similar observations were made for $r = 1000m$, as shown in Figure 4.8, where the first- and second-order approximations deviate by about 65.2 seconds in both cases. When compared to post-Newtonian expressions for propagation delay, we see that the first and second-order approximations (4.1) and (4.3) do not yield more accurate results than the post-Newtonian approach. Therefore, using them is not logical.

However, a more promising approach comes from the formula proposed by La Placa et al.[56], which uses specific values for the parameter k, as shown in Figures 4.6 - 4.8. This method works relatively well for φ between 0 and π, with good performance across all radii considered ($r = 10m$, $100m$ and $1000m$). Since this approach is more

reliable and accurate than the first- and second-order approximations, we focused on refining the values of k to achieve better accuracy, particularly for values of φ between 0 and π depending on whether the pulsar is in superior conjunction. The key question we aim to answer is whether this approach successfully reduces error. Figures 4.9, 4.10 and 4.11 show the differences between the exact and approximate delays for different k_1, k_2, and k_3 values, respectively. Table (4.1) summarizes the maximal deviations of these delays for the three considered approaches. The first line gives the delay in seconds for the assumed $4 \times 10^6 M_\odot$ solar mass black hole. The second line shows the dimensionless delay, obtained by dividing the delay by $GM/c^3 \approx 19.7\,\mathrm{s}$. The third line gives the maximal relative error. The maximal deviation from the exact delays occurs at $\varphi = \pi$.

The key for the figure below is as follows:

- Δ_{ex}: Exact propagation delay
- $\Delta_{approx.,1}$: Time delay calculated using the approximation by Beloborodov (4.1)
- $\Delta_{approx.,2}$: Time delay calculated from the approximation by Poutanen & Beloborodov (4.3)
- $\Delta_{\mathrm{approx.},3}$: Time delay calculated from the approximation by La Placa et al.(4.4)

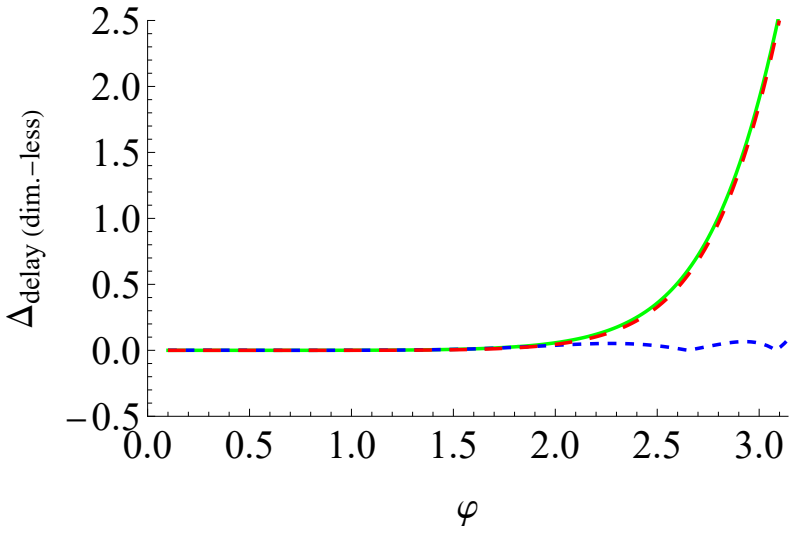

Figure 4.6: Absolute difference between the exact delay and the approximated time delays for a circular edge-on orbit with Schwarzschild radial coordinate $r = 10\,m$. The red dotted line is $\Delta_{\mathrm{ex}} - \Delta_{approx.,1}$, the green solid line $\Delta_{\mathrm{ex}} - \Delta_{approx.,2}$, the blue dashed line $\Delta_{ex} - \Delta_{\mathrm{approx.},3}$.

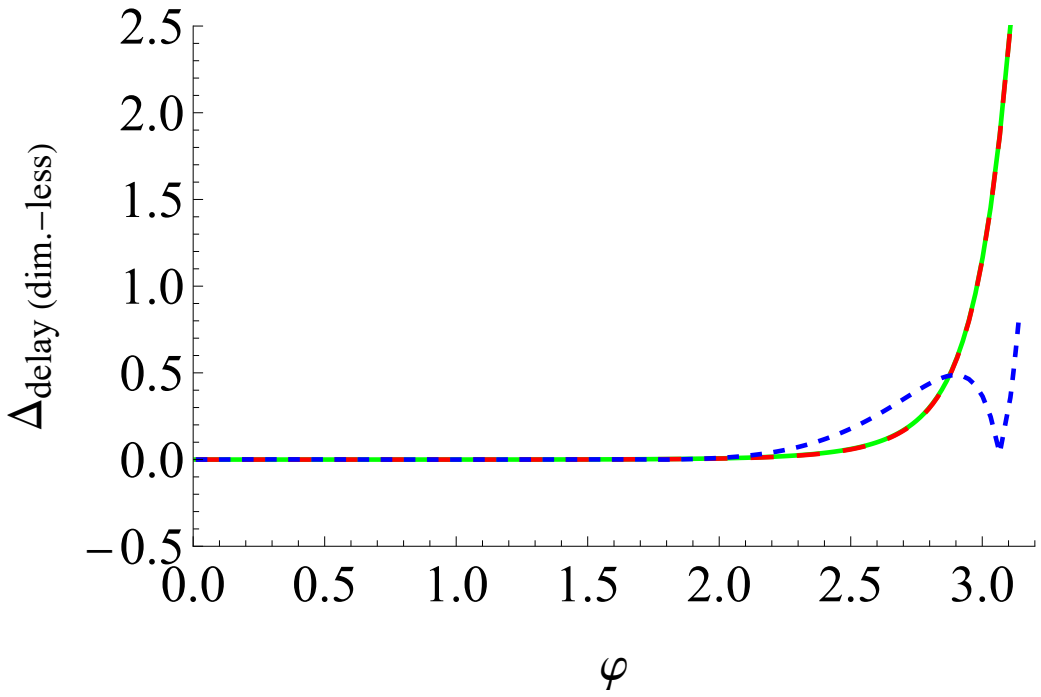

Figure 4.7: Absolute difference between the exact delay and the approximated time delays for a circular edge-on orbit with Schwarzschild radial coordinate $r = 100\,m$. The red dotted line is $\Delta_{\text{ex}} - \Delta_{approx.,1}$, the green solid line $\Delta_{\text{ex}} - \Delta_{approx.,2}$, the blue dashed line $\Delta_{ex} - \Delta_{\text{appro.},3}$.

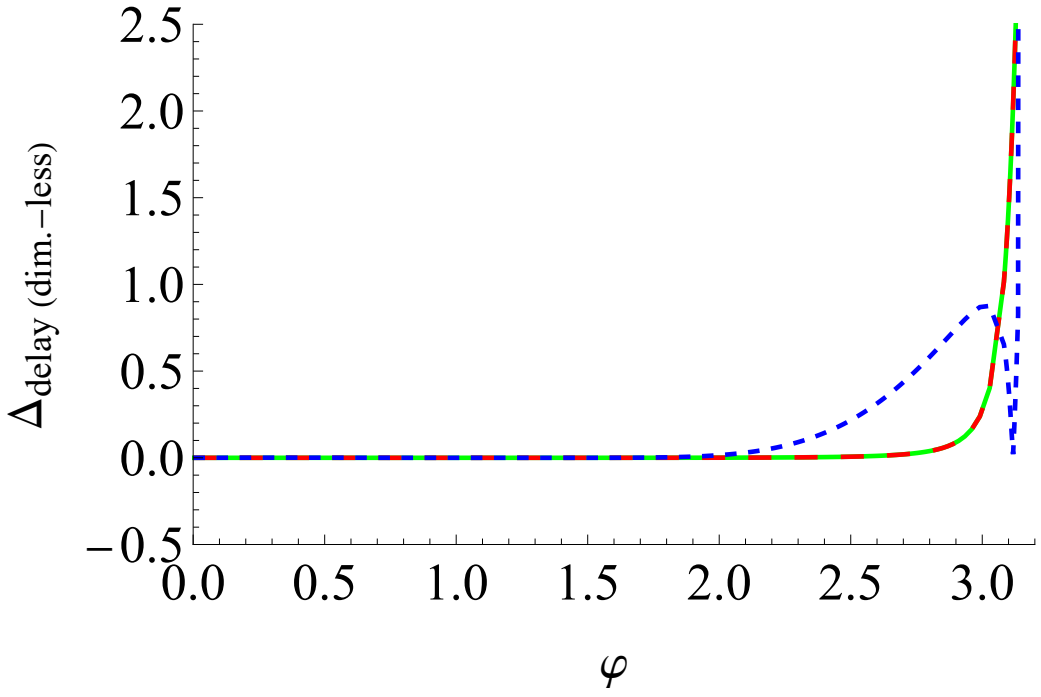

Figure 4.8: Absolute difference between the exact delay and the approximated time delays for a circular edge-on orbit with Schwarzschild radial coordinate $r = 1000\,m$. The red dotted line is $\Delta_{\text{ex}} - \Delta_{approx.,1}$, the green solid line $\Delta_{\text{ex}} - \Delta_{approx.,2}$, the blue dashed line $\Delta_{ex} - \Delta_{\text{appro.},3}$.

Table 4.1: Maximal difference $\Delta_{\text{ex}} - \Delta_{approx}$ for circular edge-on orbits with different radii r and corresponding Keplerian orbital period P.

Radius (r)	10 m	100 m	1000 m
Keplerian Period (P)	≈ 0.93 h	≈ 1.41 d	≈ 0.12 y
Delay (sec)	56.5	62.5	65.2
Delay (dim.-less)	2.87	3.18	3.31
Relative Error	3.1×10^{-1}	3.3×10^{-2}	3.3×10^{-3}

(a) Based on approximation proposed by Beloborodov

Radius (r)	10 m	100 m	1000 m
Keplerian Period (P)	≈ 0.93 h	≈ 1.41 d	≈ 0.12 y
Delay (sec)	55.6	62.4	65.2
Delay (dim.-less)	2.82	3.17	3.31
Relative Error	3.0×10^{-1}	3.3×10^{-2}	3.3×10^{-3}

(b) Based on approximation proposed by Poutanen & Beloborodov

Radius (r)	10 m	100 m	1000 m
Keplerian Period (P)	≈ 0.93 h	≈ 1.41 d	≈ 0.12 y
Delay (sec)	1.6	16.8	22.1
Delay (dim.-less)	0.08	0.85	1.12
Relative Error	6.8×10^{-3}	8.5×10^{-3}	1.1×10^{-3}

(c) Based on approximation proposed by La Placa et al.

The first line presents the delay in seconds for a black hole with an assumed mass of 4×10^6 solar masses. The second line shows this delay divided by $GM/c^3 \approx 19.7$ seconds, making it dimensionless. The third line gives the maximum relative error of the analytical approximation.

The accuracy of the propagation delays on the radius of the pulsar orbit is explored in 4.9 - 4.11, using the third approach by La Placa et al.(4.4). The analysis focuses on the third approach. Although a pulsar cannot realistically come as close as $r = 10m$ to the black hole (since it would lead to the pulsar spiraling into the black hole in a short time), we use this value for the sake of comparison. For $r = 10m$, we fit the k-values and propose $k_1 = 0.14137$, $k_2 = 1.2009$ and $k_3 = 2.7355$ which works relatively good and performs consistently as seen in Figure 4.9. To summarize the performance of our approach, we present the maximum deviation of our propagation delay calculations in Table 4.2.

Table 4.2: Maximal difference $\Delta_{\text{ex}} - \Delta_{approx}$ for circular edge-on orbits with different radii r and corresponding Keplerian orbital period P (**based on our approach**).

Radius (r)	10 m	100 m	1000 m
Keplerian Period (P)	≈ 0.93 h	≈ 1.41 d	≈ 0.12 y
Delay (sec)	2.2	1.0	1.5
Delay (dim.-less)	0.11	0.05	0.08
Relative Error	9.0×10^{-3}	5.3×10^{-4}	7.6×10^{-5}

The first line presents the delay in seconds for a black hole with an assumed mass of 4×10^6 solar masses. The second line shows this delay divided by $GM/c^3 \approx 19.7$ seconds, making it dimensionless. The third line gives the maximum relative error of the post-Newtonian approximation.

Next, for a larger value of $r = 100m$, we fit new k-values to improve the results. From Figure 4.10, we observe that the fitted line remains stable for φ ranging from 0 to π. For this case, we propose the following k-values: $k_1 = 0.12918$, $k_2 = 1.35206$, and $k_3 = 6.11555$. These values result in better accuracy within the considered range of φ. Finally, for $r = 1000m$, we again fit the k-values to optimize the results and found $k_1 = 0.15149$, $k2 = 1.49909$, and $k3 = 16.31176$. As seen in Figure 4.9, these values further improve the accuracy of the approximation by La Placa et al.(4.3).

With this analysis, we can say that by adjusting the k-values for different pulsar

orbital radii, we are able to achieve improved results for the propagation delays, particularly for values of φ in the range from 0 to π. This method shows consistent and reliable performance for different orbital radii and offers valuable insights into optimizing the analytical models for accurate pulsar timing predictions. We conclude that for edge-on orbits near superior conjunction, the approximations by Beloborodov (4.1) and Poutanen & Beloborodov (4.3) deviate significantly from the exact results and are therefore unreliable. The discrepancies between the exact propagation delay and these approximations become particularly pronounced at superior conjunction. In such cases, the values of k_1, k_2, and k_3 proposed in this work could be used as a more accurate alternative.

For slightly inclined orbits, where the pulsar is not perfectly aligned in the same plane as the observer, superior conjunction does not occur in the real sense. While the pulsar may still be positioned behind the black hole, its light will not pass as closely. Additionally, the angle φ along the pulsar's orbit no longer directly corresponds to the angle φ between the pulsar and the observer. In this scenario, the range of φ is more limited and does not reach π.

For (nearly) edge-on pulsars with high timing precision, our results indicate that using the exact timing formula (2.32) is the most reliable approach for accurately determining propagation delays.

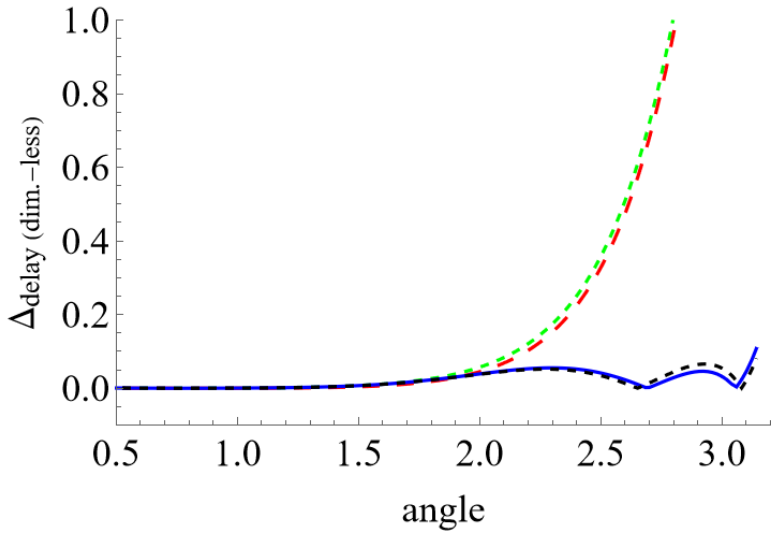

Figure 4.9: Absolute difference between the exact delay and the approximated time delays for a circular edge-on orbit with Schwarzschild radial coordinate $r = 10\,m$. The blue solid line is the fitted line. The red dashed line is $\Delta_{\text{ex}} - \Delta_{approx.,1}$, the green dashed line $\Delta_{\text{ex}} - \Delta_{approx.,2}$, the black dashed line $\Delta_{ex} - \Delta_{\text{approx.,3}}$.

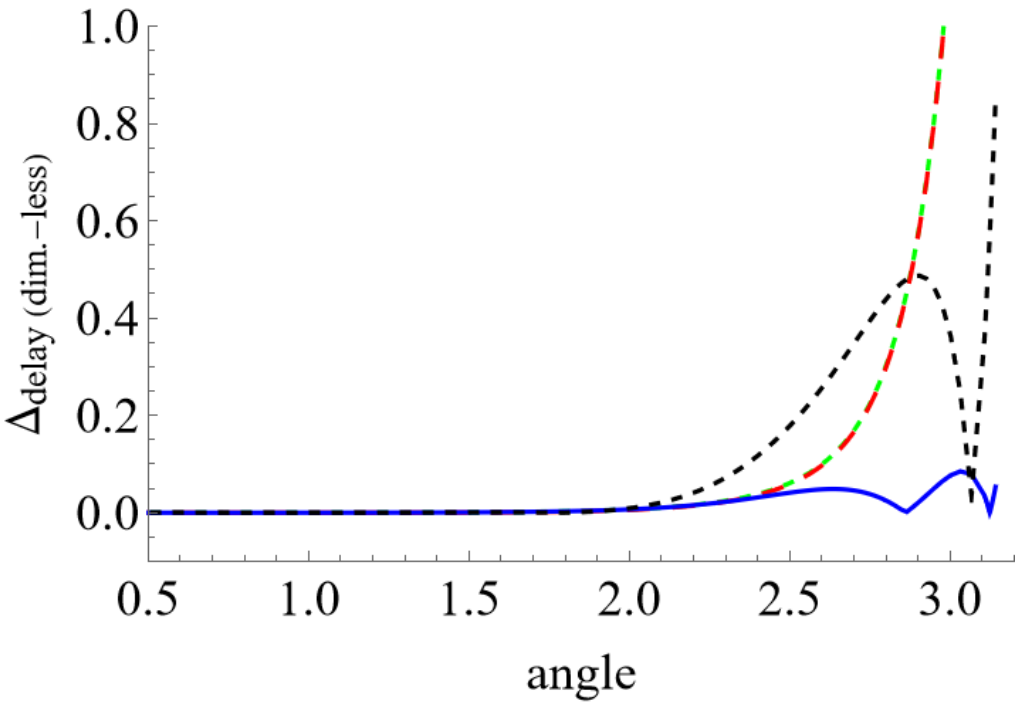

Figure 4.10: Absolute difference between the exact delay and the approximated time delays for a circular edge-on orbit with Schwarzschild radial coordinate $r = 100\,m$. The blue solid line is the fitted line. The red dashed line is $\Delta_{\text{ex}} - \Delta_{approx.,1}$, the green dashed line $\Delta_{\text{ex}} - \Delta_{approx.,2}$, the black dashed line $\Delta_{ex} - \Delta_{\text{appro.,3}}$.

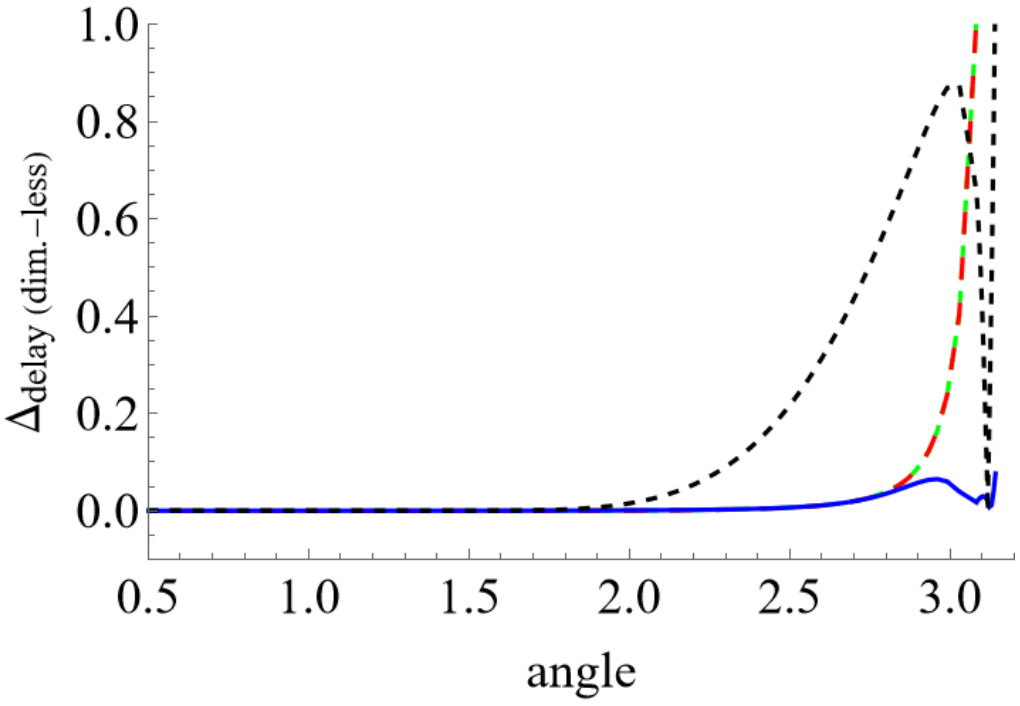

Figure 4.11: Absolute difference of the exact delay and the approximated time delays for a circular edge-on orbit with Schwarzschild radial coordinate $r = 1000\,m$. The blue solid line is the fitted line. The red dashed line is $\Delta_{\text{ex}} - \Delta_{approx.,1}$, the green dashed line $\Delta_{\text{ex}} - \Delta_{approx.,2}$, the black dashed line $\Delta_{ex} - \Delta_{\text{appro.,3}}$.

Chapter 5

Summary and Outlook

5.1 Summary

In this work, we study a pulsar orbiting a supermassive black hole due to its extreme mass ratio and investigate the propagation delays of the photon signals. The propagation delay results presented in this report can be interpreted as the relativistic delay of signals obtained by separating the diverging terms. An exact analytical solution describing lightlike geodesics and photon time delays in Schwarzschild spacetime was derived using Jacobian elliptic integrals. We obtain the solution for the emission angle, φ_e, at a fixed radius, r_e, using these integrals. The analysis we made compares exact relativistic propagation delays with approximated delays derived using three different analytical approximations. These approximations were tested for their accuracy in predicting time delays in Schwarzschild spacetime for different pulsar orbit radii, considering a black hole with a mass of 4×10^6.

Figures shows the differences between exact and approximate delays for pulsar orbits at Schwarzschild radial coordinates ($r = 10m$, $100m$, and $1000m$). The first-order and second-order approximations, particularly by Beloborodov and Poutanen et al., perform well in certain regions but fail when the pulsar is behind the black hole (in the indirect flyby orbit), deviating by up to 65.2 seconds for $r = 1000m$.

The third approach, proposed by La Placa et al., provides more consistent and accurate results across different radii. By fitting parameters k_1, k_2, and k_3, the model improves propagation delay calculations, significantly reducing errors, particularly for angles between 0 and π. Further analysis of propagation delay accuracy as a function of pulsar orbit radius shows that while small radii ($r = 10m$) are unrealistic due to the likelihood of the pulsar spiraling into the black hole, they were used for comparative purposes. The optimal k-values were determined for each radius and showed consistency. Generally, the third approximation by La Placa et al. proves to

be the most reliable, thereby balancing accuracy and efficiency well. These findings contribute to improving models for pulsar timing and light propagation in weak gravitational fields, particularly around supermassive black holes.

5.2 Further Study

The next step in this work could be to explore higher radii and different spacetimes, such as the Kerr spacetime. A major focus would be understanding how the Kerr metric influences propagation delays, particularly the frame-dragging effect and its impact on pulsar timing. [57] derived analytical expressions for bound timelike orbits in Kerr spacetime using Mino time approach [58]. This could be further investigated by considering such orbits and the corresponding relativistic effects, which would complement the results discussed here. A key challenge would be linking the motion constants of the pulsar's timelike orbit to those of the lightlike signal.

Investigating how black hole spin affects pulsar timing delays is crucial, along with developing a framework to compute and compare timing residuals for pulsars in orbits with different inclinations and parameters could be a good direction to consider. Kimpson et al. [59] investigated spin effects numerically using a light ray-tracing method but did not provide an analytical expression for the time delay in terms of orbital Kepler parameters or geodesic constants.

Additionally, a more comprehensive mathematical framework could be developed to simulate pulsar orbits in the strong-field regime around supermassive black holes. Then the resulting signal delays using high-order post-Newtonian approximations or full numerical relativity simulations. The numerical results could be compared with the weak-field predictions to analyze deviations.

Finally, higher orders of analytical approximations should be tested and compared with the exact propagation delay results to assess their accuracy and potential applicability in pulsar timing studies.

5.2.1 Limitations

Some limitations arose during the study. Some of these are listed and explained below:

- The use of Mathematica software was introduced during the internship, which affected my output at the beginning of the thesis.
- There were periods when I was somewhat skeptical about some results, especially because of my lack of prior expertise in pulsar timing, requiring additional verification to ensure accuracy.
- The results are based on theory and simulations, but real pulsar timing data is needed to confirm their accuracy.

Appendix A

Solution to the time integral

This section presents the general mathematical processes used to approximate the solution for time delay. The integral in Eq. (2.30) is of the form

$$T(r,d) = \int_{r3}^{r} \frac{r^2\,dr}{d\left(1-\frac{r_s}{r}\right)\sqrt{R(r)}} \tag{A1}$$

with $r = r_e$ or $r = \infty$, and R is defined in Eq.(2.14) where all quantities are dimensionless. The integral can be analytically solved in terms of elliptic integrals through the substitution below:

$$x^2 = \frac{(r-r_3)(r_2-r_1)}{(r-r_2)(r_3-r_1)} \tag{A2}$$

with the roots r_i of R chosen as in Eq. (2.15), which casts the integral in the Legendre form:

$$T(r,d) = \frac{2}{\sqrt{r_3(r_2-r_1)}} \int_0^{x(r)} \frac{f(x)\,dx}{\sqrt{(1-x^2)(1-k^2x^2)}} \tag{A3}$$

where

$$k^2 = \frac{r_2(r_3-r_0)}{r_3(r_2-r_0)} \tag{A4}$$

and

$$f(x) = \frac{r_2^3}{r_2-2} + \frac{A_1}{1-c_1x^2} + \frac{A_2}{1-c_2x^2} + \frac{A_3}{(1-c_3x^2)^2} \tag{A5}$$

with the constants

$$\begin{aligned} A_1 &= 2(r_3-r_2)(r_2+1), & c_1 &= \frac{r_3-r_1}{r_2-r_1}, \\ A_2 &= \frac{8(r_2-r_3)}{(r_2-2)(r_3-2)}, & c_2 &= \frac{(r_3-r_1)(r_2-2)}{(r_2-r_1)(r_3-2)}, \\ A_3 &= (r_3-r_2)^2, & c_3 &= c_1. \end{aligned} \tag{A6}$$

We note that for $r = \infty$ Eq. (A2) reduces to

$$x_\infty^2 := x(r=\infty)^2 = \frac{r_3 - r_1}{r_3 - r_1} = \frac{1}{c_1}. \tag{A7}$$

With the Jacobi elliptic integrals

$$F(x,k) = \int_0^x \frac{dx}{\sqrt{(1-x^2)(1-k^2x^2)}}, \tag{A8}$$

$$E(x,k) = \int_0^x \sqrt{(1-k^2x^2)}\, dx, \tag{A9}$$

$$\Pi(x,c,k) = \int_0^x \frac{dx}{(1-cx^2)\sqrt{(1-x^2)(1-k^2x^2)}}, \tag{A10}$$

Then, we find T(r,d) =

$$\begin{aligned} T(r,d) = \frac{2}{\sqrt{r_3(r_2-r_1)}} \Bigg[& \frac{r_2^3}{r_2-2} F(x,k) + A_1 \Pi(x,c_1,k) + A_2 \Pi(x,c_2,k) \\ & + \frac{A_3}{2(c_3-1)} \left(\frac{x c_3^2 \sqrt{(1-x^2)(1-k^2x^2)}}{(1-c_3x^2)(c_3-k^2)} + F(x,k) \right. \\ & \left. - \frac{c_3}{c_3-k^2} E(x,k) + \frac{c_3^2 + 3k^2 - 2c_3(1+k^2)}{c_3-k^2} \Pi(x,c_3,k) \right) \Bigg] \\ = \frac{2}{\sqrt{r_3(r_2-r_1)}} \Bigg[& \left(\frac{r_2^3}{r_2-2} + \frac{(r_3-r_2)(r_2-r_1)}{2} \right) F(x,k) \\ & - \frac{1}{2} r_3 (r_2-r_1) E(x,k) + 2(r_3-r_2)\Pi(x,c_1,k) \\ & - \frac{8(r_3-r_2)}{(r_3-2)(r_2-2)} \Pi(x,c_2,k) \Bigg] + \frac{d\sqrt{R(r)}}{r-r_2}, \end{aligned} \tag{A11}$$

where x is connected to r through (A2). The Jacobi elliptic integrals can be evaluated without a numeric integration, making them an exact analytical solution for the integral T.

The last term in (A11) diverges linearly as $r \to \infty$. Additionally, $\Pi(x,c,k)$ diverges logarithmically when $x^2 = \frac{1}{c}$, which occurs when $x = x_\infty$ and $c = c_1 = c_3$. As a result, the time to reach $r = \infty$ diverges as expected. To isolate the divergent

terms, we use an identity,

$$\Pi(x,c,k) = F(x,k) - \Pi\left(x, \frac{k^2}{c}, k\right) + \frac{\ln(Z)}{2P} \tag{A12}$$

where

$$Z = \frac{(1-x^2)(1-k^2x^2) + Px}{(1-x^2)(1-k^2x^2) - Px}, \tag{A13}$$

$$P^2 = \frac{(c-1)(c-k^2)}{c} = \frac{(r_3-r_2)^2}{r_3(r_2-r_1)} \tag{A14}$$

For $c = c_1$, with this Eq.(A11) becomes

$$\begin{aligned} T(r,d) = \frac{2}{\sqrt{r_3(r_2-r_1)}}\Bigg[& \left(\frac{r_2^2}{r_2-2} + \frac{1}{2}(r_3-r_2)(r_2-r_1+4)\right) F(x,k) \\ & - \frac{1}{2}r_3(r_2-r_1)E(x,k) - 2(r_3-r_2)\Pi\left(x, \frac{k^2}{c_1}, k\right) \\ & - \frac{8(r_3-r_2)}{(r_3-2)(r_2-2)}\Pi(x,c_2,k)\Bigg] + \frac{d\sqrt{R(r)}}{(r-r_2)} \\ & + 2\ln\left(\frac{\sqrt{r(r-r_1)} + \sqrt{(r-r_3)(r-r_2)}}{\sqrt{r(r-r_1)} - \sqrt{(r-r_3)(r-r_2)}}\right) \end{aligned} \tag{A15}$$

where the last two terms diverge for $x = x_\infty$. We find the Taylor expansions of these terms as

$$\frac{d\sqrt{R(r)}}{r-r_2} = r + r_2 + O\left(\frac{1}{r}\right), \tag{A16}$$

$$2\ln Z = 2\ln\left(\frac{2}{r_3+r_2}\right) + 2\ln r + O\left(\frac{1}{r}\right) \tag{A17}$$

Solution to the angle, φ

This section presents the general mathematical processes used to derive an approximate solution for φ analytically derived in terms of using the Jacobi elliptic integral.

From the polynomial $R(r)$,

$$R(r) = A(r - r_1)(r - r_0)(r - r_2)(r - r_3) \tag{A18}$$

Substitute

$$r = \frac{\beta + \alpha n x^2}{n x^2 + 1}, \quad \text{drdx} = \frac{2\alpha n x}{n x^2 + 1} - \frac{2nx\left(\beta + \alpha n x^2\right)}{\left(n x^2 + 1\right)^2} \tag{A19}$$

Divide (A18) by $drdx^2$, replace r by R, factor x, and collect terms with x.

$$R_x = \frac{A\left(\frac{\beta+\alpha n x^2}{n x^2+1} - r_1\right)\left(\frac{\beta+\alpha n x^2}{n x^2+1} - r_0\right)\left(\frac{\beta+\alpha n x^2}{n x^2+1} - r_2\right)\left(\frac{\beta+\alpha n x^2}{n x^2+1} - r_3\right)}{\left(\frac{2\alpha n x}{n x^2+1} - \frac{2nx(\beta+\alpha n x^2)}{(n x^2+1)^2}\right)^2} \tag{A20}$$

Simplify (A20) to obtain (A21)

$$\begin{aligned} R_x = \frac{A}{4n^2x^2(\alpha-\beta)^2} \cdot \left(\beta - r_1\left(n x^2 + 1\right) + \alpha n x^2\right)\left(\beta - r_0\left(n x^2 + 1\right) + \alpha n x^2\right) \cdot \\ \left(\beta - r_2\left(n x^2 + 1\right) + \alpha n x^2\right)\left(\beta - r_3\left(n x^2 + 1\right) + \alpha n x^2\right). \end{aligned} \tag{A21}$$

Choose α, β, and n with r = β and β should be one of the boundaries (zeros) of your motion. Choose $\beta = r_3$, that is, the largest zero and α as one of the other zeros which is not related to your motion. The value of n and k^2 can be derived.

Next, integrate between r_0 and r_3, with $\beta = r_3$

$$\frac{A\left(\frac{\alpha n x^2+r_3}{n x^2+1} - r_3\right)\left(\frac{\alpha n x^2+r_3}{n x^2+1} - r_1\right)\left(\frac{\alpha n x^2+r_3}{n x^2+1} - r_0\right)\left(\frac{\alpha n x^2+r_3}{n x^2+1} - r_2\right)}{\left(\frac{2\alpha n x}{n x^2+1} - \frac{2nx(\alpha n x^2+r_4)}{(n x^2+1)^2}\right)^2} \tag{A22}$$

By simplifying, factor R_x

$$\begin{aligned} \frac{A}{4n(\alpha - \mathrm{r}_3)} \cdot \left(-n\mathrm{r}_1 x^2 + \alpha n x^2 - \mathrm{r}_1 + \mathrm{r}_3\right) \\ \cdot \left(-n\mathrm{r}_0 x^2 + \alpha n x^2 - \mathrm{r}_0 + \mathrm{r}_3\right) \\ \cdot \left(-n\mathrm{r}_2 x^2 + \alpha n x^2 - \mathrm{r}_2 + \mathrm{r}_4\right). \end{aligned} \tag{A23}$$

Replace α with r_2 in (A23) and simplify

$$\frac{A\left(nr_1x^2 - nr_2x^2 + r_1 - r_3\right)\left(-r_0\left(nx^2+1\right) + nr_2x^2 + r_3\right)}{4n} \tag{A23}$$

Solve for $r_2r_3R_x =$ and factor x; we have (A24).

$$-\frac{1}{4}Anx^4(\mathrm{r_1}-\mathrm{r_2})(\mathrm{r_0}-\mathrm{r_2}) - \frac{A(\mathrm{r_1}-\mathrm{r_3})(\mathrm{r_0}-\mathrm{r_3})}{4n} - \frac{1}{4}Ax^2\left(2\mathrm{r_1r_0} - \mathrm{r_1r_2} - \mathrm{r_1r_3} - \mathrm{r_0r_2} - \mathrm{r_0r_3} + 2\mathrm{r_2r_3}\right) \tag{A24}$$

Divide the expression $r_3r_4R_x$ (A24) by its constant term (the coefficient of x^0) and then factor the resulting expression.

$$\begin{aligned}
&\frac{n^2\mathrm{r_2^2}x^4}{(\mathrm{r_1}-\mathrm{r_3})(\mathrm{r_0}-\mathrm{r_3})} - \frac{n^2\mathrm{r_1r_2}x^4}{(\mathrm{r_1}-\mathrm{r_3})(\mathrm{r_0}-\mathrm{r_3})} - \frac{n^2\mathrm{r_0r_2}x^4}{(\mathrm{r_1}-\mathrm{r_3})(\mathrm{r_0}-\mathrm{r_3})} \\
&+ \frac{n^2\mathrm{r_1r_0}x^4}{(\mathrm{r_1}-\mathrm{r_3})(\mathrm{r_0}-\mathrm{r_3})} + \frac{2nr_2r_3x^2}{(\mathrm{r_1}-\mathrm{r_3})(\mathrm{r_0}-\mathrm{r_3})} - \frac{nr_1r_2x^2}{(\mathrm{r_1}-\mathrm{r_3})(\mathrm{r_0}-\mathrm{r_3})} \\
&- \frac{nr_0r_2x^2}{(\mathrm{r_1}-\mathrm{r_3})(\mathrm{r_0}-\mathrm{r_3})} + \frac{2nr_1r_0x^2}{(\mathrm{r_1}-\mathrm{r_3})(\mathrm{r_0}-\mathrm{r_3})} - \frac{nr_1r_3x^2}{(\mathrm{r_1}-\mathrm{r_3})(\mathrm{r_0}-\mathrm{r_3})} \\
&- \frac{nr_0r_3x^2}{(\mathrm{r_1}-\mathrm{r_3})(\mathrm{r_0}-\mathrm{r_3})} + \frac{\mathrm{r_3^2}}{(\mathrm{r_1}-\mathrm{r_3})(\mathrm{r_0}-\mathrm{r_3})} + \frac{\mathrm{r_1r_0}}{(\mathrm{r_1}-\mathrm{r_3})(\mathrm{r_0}-\mathrm{r_3})} \\
&- \frac{\mathrm{r_1r_3}}{(\mathrm{r_1}-\mathrm{r_3})(\mathrm{r_0}-\mathrm{r_3})} - \frac{\mathrm{r_0r_3}}{(\mathrm{r_1}-\mathrm{r_3})(\mathrm{r_0}-\mathrm{r_3})}
\end{aligned} \tag{A25}$$

Simplifying equation (A25) gives equation (A26).

$$\frac{\left(nr_1x^2 - nr_2x^2 + r_1 - r_3\right)\left(-r_0\left(nx^2+1\right) + nr_2x^2 + r_3\right)}{(r_1-r_3)(r_3-r_0)} \tag{A26}$$

Set the coefficients of x^4 and x^2 in the equation (A26) to m and $-1-m$, respectively. We have:

$$n = \frac{-r_1 + r_3}{r_1 - r_2}, \tag{A27}$$

$$m = \frac{-r_1r_0 + r_1r_3 + r_0r_3 - r_3^2 - \frac{2r_1r_0(-r_1+r_3)}{r_1-r_2} + \frac{r_1r_2(-r_1+r_3)}{r_1-r_2} + \frac{r_0r_2(-r_1+r_3)}{r_1-r_2}}{r_1r_0 - r_1r_3 - r_0r_3 + r_3^2} + \frac{\frac{r_1r_3(-r_1+r_3)}{r_1-r_2} + \frac{r_0r_3(-r_1+r_3)}{r_1-r_2} - \frac{2r_2r_3(-r_1+r_3)}{r_1-r_2}}{r_1r_0 - r_1r_3 - r_0r_3 + r_3^2} \tag{A28}$$

Simplify (A27) and (A28)

$$n \to \frac{r_3 - r_1}{r_1 - r_2}, \quad m \to \frac{(r_1 - r_3)(r_0 - r_2)}{(r_1 - r_2)(r_0 - r_3)} \tag{A29}$$

From R, replace $\alpha \to r_2$, $\beta \to r_3$, $m \to \frac{(r_1-r_3)(r_0-r_2)}{(r_1-r_2)(r_0-r_3)}$, and $n \to \frac{r_3-r_1}{r_1-r_2}$.

$$R(r) = \frac{\frac{r_2 x^2 (r_3-r_1)}{r_1-r_2} + r_3}{\frac{x^2(r_3-r_1)}{r_1-r_2} + 1} \tag{A30}$$

Simplify (A30), we have

$$R(r) = \frac{r_1 r_2 x^2 - r_1 r_3 - r_2 r_3 x^2 + r_2 r_3}{r_1(x^2-1) + r_2 - r_3 x^2} \tag{A31}$$

From the equation (A31), substitute $x = sn\left(\sqrt{c}\varphi | k\right)$ to obtain (A32)

$$\frac{r_1 r_2\, sn\left(\sqrt{c}\varphi|k\right)^2 - r_2 r_3\, sn\left(\sqrt{c}\varphi|k\right)^2 - r_1 r_3 + r_2 r_3}{r_1\left(sn\left(\sqrt{c}\varphi|k\right)^2 - 1\right) - r_3\, sn\left(\sqrt{c}\varphi|k\right)^2 + r_2} \tag{A32}$$

Replace c in equation (A32) with $c = r_3(r_2 - r_1)/4d$

$$R(r) = \frac{r_1 r_2\, sn\left(\frac{1}{2}\sqrt{d(r_1-r_2)r_3}\,\varphi \middle| k\right)^2 - r_2 r_3\, sn\left(\frac{1}{2}\sqrt{d(r_1-r_2)r_3}\,\varphi \middle| k\right)^2 - r_1 r_3 + r_2 r_3}{-r_3\, sn\left(\frac{1}{2}\sqrt{d(r_1-r_2)r_3}\,\varphi \middle| k\right)^2 + r_1\left(sn\left(\frac{1}{2}\sqrt{d(r_1-r_2)r_3}\,\varphi \middle| k\right)^2 - 1\right) + r_2} \tag{A34}$$

Simplify (A34) to have

$$R(r) = \frac{r_2(r_1 - r_3)\, sn\left(\frac{1}{2}\sqrt{d(r_1-r_2)r_3}\,\varphi \middle| k\right)^2 + r_3(r_2 - r_1)}{(r_1 - r_3)\, sn\left(\frac{1}{2}\sqrt{d(r_1-r_2)r_3}\,\varphi \middle| k\right)^2 - r_1 + r_2} \tag{A35}$$

This is the output for $R(r)$ as a function of φ which is called the solution of φ.

Bibliography

[1] Bilel Ben-Salem and Eva Hackmann. Propagation time delay and frame dragging effects of lightlike geodesics in the timing of a pulsar orbiting SgrA*. , 516(2):1768–1780, October 2022.

[2] A. M. Ghez, S. Salim, N. N. Weinberg, J. R. Lu, T. Do, J. K. Dunn, K. Matthews, M. R. Morris, S. Yelda, E. E. Becklin, T. Kremenek, M. Milosavljevic, and J. Naiman. Measuring distance and properties of the milky way's central supermassive black hole with stellar orbits. *The Astrophysical Journal*, 689(2):1044–1062, (2008).

[3] S. Gillessen, F. Eisenhauer, S. Trippe, T. Alexander, R. Genzel, F. Martins, and T. Ott. Monitoring stellar orbits around the massive black hole in the galactic center. *The Astrophysical Journal*, 692(2):1075–1109, (2009).

[4] Ru-Sen Lu, Avery E. Broderick, Fabien Baron, John D. Monnier, Vincent L. Fish, Sheperd S. Doeleman, and Victor Pankratius. Imaging the supermassive black hole shadow and jet base of m87 with the event horizon telescope. *The Astrophysical Journal*, 788(2):120, (2014).

[5] Heino Falcke, Fulvio Melia, and Eric Agol. Viewing the shadow of the black hole at the galactic center. *The Astrophysical Journal*, 528(1):L13–L16, (1999).

[6] K. Liu, N. Wex, M. Kramer, J. M. Cordes, and T. J. W. Lazio. Prospects for probing the spacetime of sgr a* with pulsars. *The Astrophysical Journal*, 747(1):1, (2012).

[7] Dimitrios Psaltis, Norbert Wex, and Michael Kramer. A quantitative test of the no-hair theorem with sgr a* using stars, pulsars, and the event horizon telescope. *The Astrophysical Journal*, 818(2):121, February (2016).

[8] A. E. Broderick, T. Johannsen, A. Loeb, and D. Psaltis. Testing the no-hair

theorem with event horizon telescope observations of sagittarius a*. *ApJ*, 784:7, (2014).

[9] Fupeng Zhang and Prasenjit Saha. Probing the spinning of the massive black hole in the galactic center via pulsar timing: A full relativistic treatment. *The Astrophysical Journal*, 849(1):33, oct 2017.

[10] Eva Hackmann and Arnab Dhani. The propagation delay in the timing of a pulsar orbiting a supermassive black hole. *General Relativity and Gravitation*, 51(3):1–21, (2019).

[11] Tom Kimpson. Multimessenger astrophysics of pulsars in extreme mass ratio systems. 11 (2021).

[12] Alice K. Harding. The Neutron Star Zoo. *Front. Phys. (Beijing)*, 8:679–692, (2013).

[13] Victoria M. Kaspi. The Neutron Star Zoo. In P. Weltevrede, B. B. P. Perera, L. L. Preston, and S. Sanidas, editors, *Pulsar Astrophysics the Next Fifty Years*, volume 337 of *IAU Symposium*, pages 3–8, (2018).

[14] Andrea N Lommen. Pulsar timing arrays: the promise of gravitational wave detection. *Reports on Progress in Physics*, 78(12):124901, (2015).

[15] A Spolon, L Zampieri, A Burtovoi, G Naletto, C Barbieri, M Barbieri, A Patruno, and E Verroi. Timing analysis and pulse profile of the vela pulsar in the optical band from iqueye observations. *Monthly Notices of the Royal Astronomical Society*, 482(1):175–183, September 2018.

[16] J H Taylor. Binary pulsars and relativistic gravity. *The Astrophysical Journal*, (1994). VHS not held by the CERN library.

[17] M. Kramer, I. H. Stairs, R. N. Manchester, M. A. McLaughlin, A. G. Lyne, R. D. Ferdman, M. Burgay, D. R. Lorimer, A. Possenti, N. D'Amico, J. M. Sarkissian, G. B. Hobbs, J. E. Reynolds, P. C. C. Freire, and F. Camilo. Tests of General Relativity from Timing the Double Pulsar. *Science*, 314(5796):97–102, (2006).

[18] Stefano Ascenzi, Vanessa Graber, and Nanda Rea. Neutron-star measurements in the multi-messenger era, 2024.

[19] M. J. Keith, S. Johnston, A. Karastergiou, P. Weltevrede, M. E. Lower, A. Basu, B. Posselt, L. S. Oswald, A. Parthasarathy, A. D. Cameron, M. Serylak, and S. Buchner. The thousand-pulsar-array programme on meerkat xiii: Timing, flux density, rotation measure and dispersion measure timeseries of 597 pulsars, 2024.

[20] Clemente Smarra, Adrien Kuntz, Enrico Barausse, Boris Goncharov, Diana López Nacir, Diego Blas, Lijing Shao, J. Antoniadis, D.J. Champion, I. Cognard, L. Guillemot, H. Hu, M. Keith, M. Kramer, K. Liu, D. Perrodin, S.A. Sanidas, and G. Theureau. Constraints on conformal ultralight dark matter couplings from the european pulsar timing array. *Physical Review D*, 110(4), August 2024.

[21] Joris P.W. Verbiest, Sarah J. Vigeland, Nataliya K. Porayko, Siyuan Chen, and Daniel J. Reardon. Status report on global pulsar-timing-array efforts to detect gravitational waves. *Results in Physics*, 61:107719, June 2024.

[22] Reinhard Genzel, Frank Eisenhauer, and Stefan Gillessen. The galactic center massive black hole and nuclear star cluster. *Reviews of Modern Physics*, 82(4):3121–3195, (2010).

[23] Giacomo Fragione, Nathan W C Leigh, and Rosalba Perna. Black hole and neutron star mergers in galactic nuclei: the role of triples. *Monthly Notices of the Royal Astronomical Society*, 488(2):2825–2835, (2019).

[24] Chunglee Kim and Melvyn B. Davies. Neutron stars in the galactic center. *Journal of the Korean Astronomical Society*, 51(5):165–170, (2018).

[25] Eric Pfahl and Abraham Loeb. Probing the spacetime around sagittarius a* with radio pulsars. *The Astrophysical Journal*, 615(1):253, nov 2004.

[26] J. P. Macquart, N. Kanekar, D. A. Frail, and S. M. Ransom. A High-frequency Search for Pulsars within the Central Parsec of Sgr A*. , 715(2):939–946, (2010).

[27] Kaustubh Rajwade, Duncan Lorimer, and Loren Anderson. Detecting pulsars in the Galactic centre. *Mon. Not. Roy. Astron. Soc.*, 471(1):730–739, 2017.

[28] S. D. Bates, M. Bailes, N. D. R. Bhat, M. Burgay, S. Burke-Spolaor, N. D'Amico, A. Jameson, S. Johnston, M. J. Keith, M. Kramer, L. Levin, A. Lyne, S. Milia, A. Possenti, B. Stappers, and W. van Straten. The High Time Resolution Universe Pulsar Survey - II. Discovery of five millisecond pulsars. , 416(4):2455–2464, (2011).

[29] Gravity Collaboration. First Light for GRAVITY: A New Era for Optical Interferometry. *The Messenger*, 170:10–15, December 2017.

[30] Evan Keane, B Bhattacharyya, Michael Krämer, B W Stappers, S D Bates, M Burgay, S Chatterjee, D J Champion, R P Eatough, J W T Hessels, G Janssen, K J Lee, J van Leeuwen, J. Margueron, M Oertel, Andrea Possenti, S Ransom, G. Theureau, and P Torne. A Cosmic Census of Radio Pulsars with the SKA. *PoS*, AASKA14:040, 2015.

[31] Walid A. Majid, Aaron B. Pearlman, Kenzie Nimmo, Jason W. T. Hessels, Thomas A. Prince, Charles J. Naudet, Jonathon Kocz, and Shinji Horiuchi. A dual-band radio observation of frb 121102 with the deep space network and the detection of multiple bursts. *The Astrophysical Journal Letters*, 897(1):L4, jun 2020.

[32] Joris PW Verbiest, Matthew Bailes, W van Straten, George B Hobbs, Russell T Edwards, Richard N Manchester, NDR Bhat, John M Sarkissian, Bryan A Jacoby, and Shri R Kulkarni. Precision timing of psr j0437–4715: an accurate pulsar distance, a high pulsar mass, and a limit on the variation of newton's gravitational constant. *The Astrophysical Journal*, 679(1):675, (2008).

[33] Michael Kramer. Probing gravitation with pulsars. *Proceedings of the International Astronomical Union*, 8(S291):19–26, (2012).

[34] K. Liu, J. P. W. Verbiest, M. Kramer, B. W. Stappers, W. van Straten, and J. M. Cordes. Prospects for high-precision pulsar timing: Psr j04374715 profile

stability. *Monthly Notices of the Royal Astronomical Society*, 417(4):2916–2926, September 2011.

[35] J. M. Cordes and R. M. Shannon. A measurement model for precision pulsar timing, 2010.

[36] D. Nice, P. Demorest, I. Stairs, R. Manchester, J. Taylor, W. Peters, J. Weisberg, A. Irwin, N. Wex, and Y. Huang. Tempo: Pulsar timing data analysis. Astrophysics Source Code Library, record ascl:1509.002, September 2015.

[37] George Hobbs, R. Edwards, and R. Manchester. Tempo2, a new pulsar timing package. 1. overview. *Mon. Not. Roy. Astron. Soc.*, 369:655–672, 2006.

[38] Jing Luo, Scott Ransom, Paul Demorest, Paul S. Ray, Anne Archibald, Matthew Kerr, Ross J. Jennings, Matteo Bachetti, Rutger van Haasteren, Chloe A. Champagne, Jonathan Colen, Camryn Phillips, Josef Zimmerman, Kevin Stovall, Michael T. Lam, and Fredrick A. Jenet. Pint: A modern software package for pulsar timing. *The Astrophysical Journal*, 911(1):45, apr 2021.

[39] Joseph H. Taylor and Joel M. Weisberg. Further experimental tests of relativistic gravity using the binary pulsar psr 1913+16. *The Astrophysical Journal*, 345:434–450, 1989.

[40] Paulo C. C. Freire. Tests of gravity theories with pulsar timing, 2022.

[41] Ingrid H. Stairs. Testing general relativity with pulsar timing. *Living Reviews in Relativity*, 6(1), September 2003.

[42] P. C. C. Freire and N. Wex. Gravity experiments with radio pulsars. *Living Reviews in Relativity*, 27(1), 2024.

[43] T. Damour and N. Deruelle. General relativistic celestial mechanics of binary systems. I. The post-newtonian motion. *Annales de l'I.H.P. Physique théorique*, 43(1):107–132, 1985.

[44] Irwin I. Shapiro. Fourth Test of General Relativity. *Phys. Rev. Lett.*, 13:789–791, (1964).

[45] R. Blandford and S. A. Teukolsky. Arrival-time analysis for a pulsar in a binary system. , 205:580–591, (1976).

[46] V. Brumberg. *Essential Relativistic Celestial Mechanics*. CRC Press, 1st edition, (1991).

[47] Sven Zschocke and Sergei A. Klioner. Analytical solution for light propagation in schwarzschild field having an accuracy of 1 micro-arcsecond, (2009).

[48] Roman R. Rafikov and Dong Lai. Effects of gravitational lensing and companion motion on the binary pulsar timing. *Phys. Rev. D*, 73:063003, Mar 2006.

[49] Event Horizon Telescope Collaboration et al. First m87 event horizon telescope results. i. the shadow of the supermassive black hole. *arXiv preprint arXiv:1906.11238*, (2019).

[50] Eva Hackmann. Introduction to general relativity. pages 53–64, (2017).

[51] K. R. Pechenick, C. Ftaclas, and J. M. Cohen. Hot spots on neutron stars - The near-field gravitational lens. , 274:846–857, (1983).

[52] Dong Lai and Roman R. Rafikov. Effects of gravitational lensing in the double pulsar system j0737-3039. *The Astrophysical Journal*, 621(1):L41–L44, February 2005.

[53] J. Schneider. Gravitational beam deviation effects in the timing formula of binary pulsars. , 232:62, June 1990.

[54] Andrei M. Beloborodov. Gravitational bending of light near compact objects. *The Astrophysical Journal*, 566(2):L85–L88, February 2002.

[55] J. Poutanen and A. M. Beloborodov. Pulse profiles of millisecond pulsars and their fourier amplitudes. *Monthly Notices of the Royal Astronomical Society*, 373(2):836–844, December 2006.

[56] Riccardo La Placa, Pavel Bakala, Luigi Stella, and Maurizio Falanga. A new approximation of photon geodesics in schwarzschild spacetime. *Research Notes of the AAS*, 3(7):99, July 2019.

[57] Ryuichi Fujita and Wataru Hikida. Analytical solutions of bound timelike geodesic orbits in kerr spacetime. *Classical and Quantum Gravity*, 26(13):135002, June 2009.

[58] Yasushi Mino. Perturbative approach to an orbital evolution around a supermassive black hole. *Phys. Rev. D*, 67:084027, Apr 2003.

[59] Kimpson, T., Wu, K., and Zane, S. Radio timing in a millisecond pulsar – extreme/intermediate mass ratio binary system. *AA*, 644:A167, 2020.

Acknowledgements

I, Ifeoma Mavis Akpuogwu acknowledge support through [1] funded by the European Union in the framework of the Erasmus+, Erasmus Mundus Joint Master in Astrophysics and Space Science – MASS. I would like to express my gratitude to my supervisors PD Dr. Eva Hackmann and Prof. Bojan Arbutina, for their unwavering support and guidance throughout the thesis period. I am also grateful for the support of all group members who I have had to ask questions at one point or another. Lastly, I am profoundly grateful to God, my family and friends for their unwavering support in this journey.

[1] "Erasmus Mundus Joint Master (EMJM)" scholarship

Declaration of Authorship

I hereby affirm that I have written the present work independently and have used no sources or aids other than those indicated. All parts of my work that have been taken from other works, either verbatim or in terms of meaning, have been marked as such, indicating the source. The same applies to drawings, sketches, pictorial representations and sources from the Internet, including AI-based applications or tools. The work has not yet been submitted in the same or a similar form as a final examination paper.

Declaration regarding the publication of master's thesis

I agree that my thesis may be viewed by third parties in the university archive for academic purposes.
I agree that my thesis may be viewed by third parties for academic purposes in the university archive after 30 years (in accordance with §7 para. 2 BremArchivG).

Declaration of consent for electronic checking of the work for plagiarism

I agree that the work I have submitted and written will be stored permanently on the external server of the plagiarism software currently used by the University of Bremen, in a library belonging to the institution (accessed only by the University of Bremen), for the above-mentioned purpose.

With my signature, I confirm that I have read and understood the above explanations and confirm the accuracy of the information provided.

Ifeoma Mavis Akpuogwu,

Date: 13.02.2025 Signature: